The within-subject application of diffusion tensor MRI and CLARITY reveals brain structural changes in *Nrxn2* deletion mice

Eleftheria Pervolaraki Ph.D[1]*, Adam L. Tyson MRes[2,3,4]*, Francesca Pibiri Ph.D[5], Steven L. Poulter Ph.D[5], Amy C. Reichelt Ph.D[6], R. John Rodgers Ph.D[7], Steven J. Clapcote Ph.D[1], Colin Lever Ph.D[5], Laura C. Andreae MBBS Ph.D[2,3]*, James Dachtler Ph.D[1,5]*

[1]School of Biomedical Sciences, University of Leeds, LS2 9JT, UK

[2]Centre for Developmental Neurobiology, Institute of Psychiatry, Psychology and Neuroscience, King's College London, London SE1 1UL, UK

[3]MRC Centre for Neurodevelopmental Disorders, King's College London, London SE1 1UL, UK

[4]Department of Forensic and Neurodevelopmental Sciences, Institute of Psychiatry, Psychology and Neuroscience, King's College London, London SE5 8AF, UK

[5]Department of Psychology, Durham University, South Road, Durham, DH1 3LE, UK

[6]Robarts Research Institute, Western University, London, Ontario, Canada, N6A 5B7, Canada

[7]School of Psychology, University of Leeds, LS2 9JT, UK

*These authors contributed equally.

Address for Correspondence: Dr J Dachtler, Department of Psychology, Durham University, South Road, Durham, DH1 3LE, UK. Email: james.dachtler@durham.ac.uk

Abstract

Background

Of the many genetic mutations known to increase the risk of autism spectrum disorder, a large proportion cluster upon synaptic proteins. One such family of presynaptic proteins are the neurexins (NRXN), and recent genetic and mouse evidence has suggested a causative role for *NRXN2* in generating altered social behaviours. Autism has been conceptualised as a disorder of atypical connectivity, yet how single-gene mutations affect such connectivity remains under-explored. To attempt to address this, we have developed a quantitative analysis of microstructure and structural connectivity leveraging diffusion tensor MRI (DTI) with high-resolution 3D imaging in optically cleared (CLARITY) brain tissue in the same mouse, applied here to the *Nrxn2α* knockout (KO) model.

Methods

Fixed brains of *Nrxn2α* KO mice underwent DTI using 9.4T MRI, and diffusion properties of socially-relevant brain regions were quantified. The same tissue was then subjected to CLARITY to immunolabel axons and cell bodies, which were also quantified.

Results DTI revealed decreases in fractional anisotropy and increases in apparent diffusion coefficient in the amygdala (including the basolateral nuclei), the anterior cingulate cortex, the orbitofrontal cortex and the hippocampus. Radial diffusivity of the anterior cingulate cortex and orbitofrontal cortex was significantly increased in *Nrxn2α* KO mice, as were tracts between the amygdala and the orbitofrontal cortex. Using CLARITY, we

find significantly altered axonal orientation in the amygdala, orbitofrontal cortex and the anterior cingulate cortex, which was unrelated to cell density.

Conclusions

Our findings demonstrate that deleting a single neurexin gene (*Nrxn2α*) induces atypical structural connectivity within socially-relevant brain regions. More generally, our combined within-subject DTI and CLARITY approach presents a new, more sensitive method of revealing hitherto undetectable differences in the autistic brain.

Key Words

MRI, CLARITY, social, autism, axons, diffusion, structure, imaging

Background

Autism is a common neurodevelopmental disorder, which is highly heritable (1). While heritability is high, it is also clear that autism is highly polygenic. Around ~400-1000 genes are involved in autism susceptibility (2-5). Many of these genes cluster upon proteins relating to synaptic signaling (6). A family of presynaptic proteins garnering recent interest have been the neurexins (*NRXNs*). NRXNs are encoded by three genes (*NRXN1, NRXN2, NRXN3;* note that *CNTNAP1* and *CNTNAP2* are sometimes referred to as *NRXN4*), of which two major isoforms exist: the longer α proteins with six laminin/neurexin/sex hormone (LNS) binding domains, and the shorter β proteins with one LNS binding domain (7, 8).

Mutations within all three *NRXN* genes have been linked to autism (6). Heterozygous deletions within *NRXN2* have been identified in a number of individuals with autistic phenotypes. These include an autistic boy and his father (who had severe language delay but not autism) who both had a frameshift mutation within exon 12 of *NRXN2* (9); a 570-kb de novo deletion of 24 genes at chromosome 11q13.1, including *NRXN2*, in a 21-year old man displaying a clinical phenotype including autistic traits (10); a 1.6Mb deletion at chromosome region 11q12.3-11q13.1, including *NRXN2*, in a 23-year old man with intellectual disability and behavioral problems (11); a de novo frameshift mutation identified in a Chinese man with autism spectrum disorder (ASD) (12), a 921 kb microdeletion at 11q13 in a 2 year old boy who had language and developmental delay (although did not meet the autism diagnosis criteria) (13) and a paternally inherited microRNA miR-873-5p variant in an ASD individual which altered binding affinity for several risk-genes including *NRXN2* and *CNTNAP2* (*NRXN4*) (14). Furthermore, recently, two large-scale reports have identified *NRXN2* with ASD risk. A study of 529 ASD patients and 1,923 controls in a Chinese population identified two *NRXN2* variants which significantly increase ASD risk (15). The second study employed machine learning approaches across 5000 ASD families to rank the importance of ASD candidate genes, and ranks *NRXN2* in the top ~0.5% of genes, i.e. 113th (16). For comparison, *NRXN1*, for which the evidence base for its links to ASD is broader and stronger, ranks 45, and *CNTNAP2* ranks 211th (16). Consistent with these association studies, we and others have previously found that homozygous or heterozygous deletion of *Nrxn2*α induces impairment in social approach and social recognition (17-19). In

summary, although mutations within *NRXN2* are rare, understanding how they may drive social, ASD-relevant behavioural changes is important. One important goal is to help elucidate how apparently convergent pathophysiology in ASD emerges despite marked genetic heterogeneity (Insert ref Geschwind & State, 2015 cited above); mapping brain alterations driven by different single genes is thus a crucial task.

Currently it is unknown whether deletion of *Nrxn2α* changes the brain's microstructure and connectivity. One previous study found coarse alterations to cell layer thickness within the hippocampus of *Nrxn2α* homozygous KOs (20). However, cell density measurements are unlikely to reveal the true extent of changes within the autistic brain. Within the current study, we have addressed this by developing a dual imaging approach (DTI and CLARITY) that quantifies the alignment and density of white matter, applied here to brain regions known to support social behavior in a mouse model of autism.

Diffusion tensor MRI (or DTI) is based upon the movement of water molecules, a measure that is termed fractional anisotropy (FA). Apparent diffusion coefficient (ADC) is similar to FA, but quantifies diffusion restriction as opposed to the spatial symmetry of diffusion. This approach has been used to explore neuropathological markers in autistic patients; alterations in myelination, axonal abundance, size and orientation all modify FA and ADC values (21-23). Using the preferred direction of the diffusion of tensors between brain regions can be used to explore their potential connection. Quantification of those computed streamlines by FA and axial and/or radial

diffusion can indicate impairments in regional structural connectivity. Since aberrant brain connectivity is likely a core feature of autism (24), we reasoned that the candidate method for probing the autistic brain should combine tractographic techniques. Accordingly, here, we combined high resolution imaging of labelled neuronal tracts in brains rendered transparent by CLARITY with DTI.

CLARITY is a recent development that renders tissue optically transparent and macromolecule permeable (25). This permits antibody staining and imaging of much larger tissue volumes than possible under traditional immunofluorescence techniques. By examining fiber orientation without sectioning-related artefacts and biases, axonal staining in cleared tissue affords a deeper understanding of the microstructure and structural connectivity of a brain region.

Given the social impairments found within *Nrxn2α* mice, we sought to examine those brain regions most closely linked with social behavior (See Supplemental Materials). Briefly, we identified four regions of interest (ROIs): the amygdala, and three brain regions strongly and directly connected to the amygdala; the hippocampus, orbitofrontal cortex (OFC), and anterior cingulate cortex (ACC). As predicted, structural connectivity was abnormal in *Nrxn2α* mice.

Methods

Ethics

153 All procedures were approved by the University of Leeds and Durham
154 University Animal Ethical and Welfare Review Boards and were performed
155 under UK Home Office Project and Personal Licenses in accordance with the
156 Animals (Scientific Procedures) Act 1986.
157
158 **Animals**
159 Full details of the animals, their background, genotyping and housing can be
160 found elsewhere (17). In brief, male B6;129-
161 *Nrxn3tm1Sud*/*Nrxn1tm1Sud*/*Nrxn2tm1Sud*/J mice (JAX #006377) were
162 purchased from the Jackson Laboratory and outbred once to the
163 C57BL/6NCrl strain (Charles River, Margate, United Kingdom) to obtain mice
164 that were individually Nrxn2α KO heterozygotes. Subsequently, HET knockout
165 males were bred with HET females (cousin mating).
166
167 **Experimental animals**
168 6 adult wild-type males (Charles River, Margate, UK) and 6 age matched
169 littermate Nrxn2α KO homozygotes (71 days ± 6 days old (SEM)) were
170 perfused-fixed with 4% paraformaldehyde (PFA) in 0.1 M phosphate buffer
171 saline (PBS) and the brains extracted. The brains were immersed in 4%
172 PFA/0.1 M PBS for a minimum of 48 hours prior to imaging. During imaging,
173 the samples were placed in custom-built MR-compatible tubes containing
174 Fomblin Y (Sigma, Poole, Dorset, UK).
175
176 Due to the relatively low variance, and owing to the complexity and
177 methodological nature in our experimental approach, we achieved

significance by groups of 6 (power provided in Results). No data was excluded from the study. Sample randomisation was performed by JD, with experimenters (EP and ALT) blinded to genotype.

Data Acquisition

Image acquisition has been described elsewhere (26). Each brain was 3D imaged using the protocol TE: 35 ms, TR: 700 ms and 10 signal averages. The field of view was set at 128 x 128 x 128, with a cubic resolution of 100 μm/pixel and a b value of 1200 s/mm^2. Further details can be found in Supplemental Materials.

Image Processing

Parsing of the raw data was semi-automated using DSI Studio, in order to obtain b-values for every normalized gradient vector on the x, y and z orientations. Unwanted background, setting a threshold, smoothing of the data and definition of tissue boundaries was performed prior to the reconstruction of the final 3D image. DTI analysis parameters were calculated as previously described (28).

The *ex vivo* mouse brain 3D diffusion-weighted images were reconstructed from the Bruker binary file using DSI Studio (http://dsi-studio.labsolver.org) (29). Direction Encoded Colour Map (DEC) images were generated by combining the information from the primary eigenvectors, diffusion images and the FA. Images of the primary vectors and their orientation were

reconstructed and superimposed on corresponding FA images to guide the segmentation of discrete anatomical locations according to the brain atlas (Figure 1B-D). Region of interest definition was performed by author EP and corroborated independently by JD, with region area compared between the experimenters (data not shown). We identified a canonical coronal slice (100 µm) for a given ROI from the standard mouse brain atlas (Figure 1A-D; Supp. Figure 1) (27). We analysed three coronal slices centred on the canonical slice, totalling 300 µm in anterior/posterior extent. For whole brain region analysis, we used a similar approach, except regions were segmented for every other slice in the anterior to posterior extent. The DSI Studio DTI reconstruction characterizes the major diffusion direction of the fibre within the brain (30, 31). Extraction of FA (calculated (26)) and ADC was performed within selected segmented brain areas for every 3D reconstructed mouse brain.

Regions of Interest (ROIs)

Our DTI approach was to undertake an *a posteriori* analysis of neural organization in regions of interest (ROIs) identified by previous literature as socially-relevant. Given the social impairments found within *Nrxn2*α mice, for the current study, we identified the brain regions of interest (ROIs) most closely linked with social behavior, using previously published reports of brain region involvement in social behaviour. Quantification of c-Fos immunoreactivity has highlighted the importance of several amygdala nuclei (including the basolateral) following social exposure (32), but also the anterior cingulate cortex (ACC), prefrontal cortex and the hippocampus (33). Lesions

to the primate amygdala alter social interactions (34, 35), and amygdala neurons in primates including humans increase firing rates during social scenarios (36-38). Consistent with these animal studies, amygdala damage in humans (39) and amygdala dysfunction in ASD patients (40) impair social responses. Other socially-important brain regions have also been proposed. Notably, several studies have implicated the rodent hippocampus in social behavior, including social memory and sociability (41-43). For instance, intrahippocampal administration of neurolide-2, which interacts with α-neurexin, specifically impairs sociability, but not anxiety and spatial learning in rats (44). These findings are consistent with reports of social deficits in humans with hippocampal damage (45) and hippocampal abnormalities in ASD (46, 47). Finally, several studies link the frontal cortex, particularly the orbitofrontal cortex, which is strongly anatomically connected with the amygdala(48), to social processing (49, 50), consistent with findings of abnormalities in orbitofrontal cortex in ASD (48, 51). Control regions of the primary motor cortex (M1), primary sensory cortex (S1) and the barrel field were chosen for CLARITY (Supp. Figure 12N-O).

CLARITY

Following MR imaging, the brains were washed in PBS to remove all Fomblin Y and then incubated for 7 days in hydrogel solution at 4°C prior to polymerisation at 37°C for 3.5 hours. The tissue was cut into 1.5 mm coronal sections using a custom 3D-printed brain-slicing matrix based on MRI scans of an adult C57BL/6 mouse brain (52) and incubated in clearing buffer for 24 days at 37°C with shaking. The cleared tissue was then washed in $PBSTN_3$

(0.1% TritonX-100 and 1.5 mM sodium azide in PBS) for 24 hours at room temperature and incubated in primary antibody solution (neurofilament (Aves NF-H) 1:100 in $PBSTN_3$) at 37°C with shaking for 13 days. Samples were washed, and then incubated in secondary antibody (AlexaFluor 488 goat anti-chicken IgY) as per the primary. Sections were washed again, and incubated in 3.6 µM DAPI (4',6-diamidino-2-phenylindole) followed by 85% glycerol in PBS for refractive index matching.

Cleared samples were imaged using a Zeiss 7MP multiphoton microscope at 770 nm using a 20x objective lens (W Plan-Apochromat, NA 1.0, WD 1.7 mm). Images (512 x 512 x 512 voxels or 265 x 265 x 265 µm with an isotropic resolution of 520 nm) were acquired in ACC, basolateral (BLA) and basomedial amygdala and OFC) in both hemispheres. DAPI and neurofilament signal was segmented into cell nuclei and axons, and the resulting binary images were used to generate values for cell density, axonal density and axonal alignment.

Full CLARITY methodological details are available within Supplemental Materials.

Data Availability

Codes to analyse CLARITY datasets are made available by author LCA by email request to either JD or LCA, subject to reference to the current paper. The datasets used and/or analysed during the current study are available from the corresponding author on reasonable request.

278

279 **Data Analysis**

280 All data are expressed as mean ± standard error of the mean (SEM). To
281 assess the variance between genotypes within a single brain structure across
282 hemispheres (given the importance of hemispheric differences in ASD (53)),
283 data was analyzed by within subject repeated measures two-way ANOVAs,
284 with Sidak multiple corrections employed on post hoc testing, or unpaired T-
285 tests. To correct for multiple comparisons, we employed the Benjamini-
286 Hochberg Procedure (corrected P values stated). Non-significant statistical
287 results, particularly hemisphere comparisons, can be found in Supplemental
288 Materials. Statistical testing and graphs were made using GraphPad Prism
289 version 6 and SPSS v22.

290

291 **Results**

292 ***Nrxn2α* deletion disrupts DTI measures of microstructure in social brain**
293 **regions**

294 To assess whether *Nrxn2α* deletion alters gross morphology, we quantified
295 whole brain volume using DTI. We found total brain volume for wild-types and
296 *Nrxn2α* KOs was similar (456.0 ± 14.76 vs. 466.2 ± 11.0 mm^3 (respectively);
297 $t_{(10)} = 0.55$, $p = 0.59$). Thus, Nrxn2α deletion does not change total brain size.

298

299 To quantitatively measure DTI, we examined FA and ADC. FA analyses
300 changes in the linear orientation (i.e. along an axonal tract), whereas ADC
301 (mean diffusivity) averages diffusion in all directions (i.e. the X, Y and Z axis),
302 which is sensitive to changes such as altered alignment. The amygdala is

critically important for social behaviours. To assess whether amygdalar alterations might account for social impairments in Nrxn2α KO mice, we segmented the whole amygdala structure and the basolateral nuclei along the anterior-posterior axis.

The posterior amygdala showed a significant reduction in FA in *Nrxn2α* KO mice (Figure 2A-B) (anterior: genotype ($F_{(1, 10)}$ = 5.81, p = 0.056); posterior: genotype ($F_{(1, 10)}$ = 11.2, p = 0.025, power = 85.4%)). This FA reduction was also observed specifically in the BLA, a region strongly associated with social behaviours (Figure 2C; genotype ($F_{(1, 10)}$ = 6.31, p = 0.049, power = 62.1%)). ADC was not significantly altered in the anterior amygdala, posterior amygdala or BLA (Figure 2D-F; all genotype: $F_{(1, 10)}$ <1).

We conducted the same analysis for the two prefrontal regions implicated in social behaviour and autism: the OFC and ACC. The pattern of results was similar for both regions: FA was not altered, while ADC was increased in the OFC (Figure 3A-B) and the ACC (Figure 3C-D). FA for the OFC was not significantly altered (genotype: ($F_{(1, 10)}$ = 3.04, p = 0.079)) but ADC was significantly increased (genotype: ($F_{(1, 10)}$ = 8.20, p = 0.043, power = 73.3%)). The ACC was unaltered in FA ($t_{(10)}$ = 1.70, p = 0.08) but had significantly increased ADC ($t_{(10)}$ = 7.52, p = 0.002, power = 99.9%).

We sought to examine whether changes in the amygdala (Supp. Figure 4), OFC or ACC FA and ADC were driven by diffusion in the primary axis (λ_1) or the radial orientations (λ_2 and λ_3) by characterisation of AD (primary) and RD

(radial). Within the OFC (Figure 3E-F), AD was significantly increased (genotype: ($F_{(1, 10)}$ = 10.74, p = 0.029, power = 83.9%)), as was RD (genotype: ($F_{(1, 10)}$ = 18.26, p = 0.009, power = 97.0%)), suggesting that both along-tract diffusion and tract branching were affected. However, in the ACC (Figure 3G-H), only RD was significantly increased ($t_{(10)}$ = 5.65, p = 0.007, power = 99.9%), with no alteration in AD ($t_{(10)}$ = 1.69, p = 0.09). Increased RD is thought to reflect demyelination or changes in axonal density or orientation (54).

DTI reveals altered hippocampal microstructure in *Nrxn2α* KO mice

The hippocampus has recently been associated with social motivation and social recognition. Since the specific contributions of the dorsal and ventral hippocampal poles remain unclear, we segmented the whole hippocampus into anterior (Bregma -1.94 mm), middle (Bregma -2.46 mm) (both dorsal) and posterior (Bregma -3.28 mm) (incorporating ventral regions) levels.

FA values in the anterior, mid and posterior hippocampus were not significantly altered (see Supp. Table 1 for statistics and Supp. Figure 5A-C). Similarly, ADC was unaltered for the anterior and mid hippocampus (Supp. Table 1 for statistics and Supp. Figure 5D-E), but was significantly increased in *Nrxn2α* KO mice in the posterior hippocampus (genotype: ($F_{(1, 10)}$ = 8.80, p = 0.036, power = 76.6%); Supp. Figure 5F). There were no significant genotype differences in AD in any of the hippocampal regions (Supp. Figure 6A-C). However, RD was significantly increased in the posterior hippocampus in *Nrxn2α* KO mice (genotype: ($F_{(1, 10)}$ = 10.83, p = 0.027, power = 84.2%;

353 Supp. Figure 6F) but not in anterior and mid regions (see Supp. Table 1;
354 Supp. Figure 6D-E). The theoretical approach undertaken hitherto was to
355 segment ROIs using a single coronal plane (as outlined in the Methods),
356 which subsequently allowed for the same anterior/posterior region to be
357 analysed by CLARITY. However, this restricted analysis could theoretically
358 miss diffusion differences across a whole brain region (as in, for example, the
359 entire anterior to posterior ACC). As a further quantification, we segmented
360 whole regions for the amygdala (Supp. Figure 7), the anterior and posterior
361 hippocampus (Supp. Figure 8) and the OFC and ACC (Supp. Figure 9). We
362 found that although there were more statistical differences between the
363 genotypes for the 'whole' anterior hippocampus region compared to the
364 'single plane' analysis, overall the two analysis methods suggested broadly
365 similar structural alterations.
366
367 Lastly, given DTI is most commonly associated with analysis of white matter
368 tracts, we also quantified the corpus callosum. Changes within the corpus
369 callosum have repeatedly been highlighted in autism (55, 56), including
370 mouse models of autism (57, 58). Here, we found significantly increased FA
371 and reduced ADC in *Nrxn2α* KO mice, which were driven by a significant
372 reduction in RD (Supp. Figure 10).
373
374 In summary, the microstructural measures most altered by *Nrxn2α* deletion
375 were increases in ADC and RD, including in the hippocampus, in line with
376 recent work suggesting a role for ventral hippocampus in social memory (43).
377

DTI tractography reveals *Nrxn2α* deletion affects strucutral connectivity between the amygdala and orbitofrontal cortex

The amygdala is strongly and bidirectionally connected to both the hippocampus (59) and the OFC (60). As all three regions are themselves important for social behaviour, and autism is thought to be, at least in part, related to abnormal structural connectivity (24), we performed tractography analysis between the amygdala (and specifically the BLA) and the hippocampus, and between the amygdala and the OFC.

From the anterior amygdala, we examined the diffusivity (AD and RD) of connections to the anterior and posterior hippocampus (Supp. Figure 11). We did not observe differences in RD in the tracts connecting the amygdala with the hippocampus (see Supp. Table 2 for non-significant statistics). Although AD between the anterior amygdala and anterior hippocampus did not differ by genotype, there was a significant interaction between genotype and hemisphere (genotype x hemisphere ($F_{(1, 10)}$ = 12.12, p = 0.023, power = 88.0%; Figure 4A); post hoc analysis shows this was driven by larger right-vs-left hemisphere AD values within the *Nrxn2α* KOs only (p = 0.012). This difference could be driven by the BLA; there was increased AD in both the BLA/anterior hippocampus tracts (genotype x hemisphere ($F_{(1, 10)}$ = 10.53, p = 0.032, power = 83.2%) and the BLA/posterior hippocampus tracts (genotype x hemisphere ($F_{(1, 10)}$ = 12.97, p = 0.020, power = 90%), which again was related to larger right-vs-left hemisphere values in the *Nrxn2α* KOs (BLA/anterior hippocampus: p = 0.004 and BLA/posterior hippocampus: p = 0.001, (Figure 4C-D)) but not the wild-type (anterior: p = 0.87; posterior: p =

1.00). These results indicate that there are differences for the structural connectivity of the amygdala with the hippocampus within the left and right hemisphere in *Nrxn2α* KO mice, with increased axial diffusivity in the right hemisphere. This finding is particularly interesting, as hemispheric differences in functional connectivity, particularly affecting connections from the right amygdala, have been found children with ASD (61, 62).

Finally, we tested connections between the amygdala and the OFC. For AD, wild-type and Nrxn2α KO mice did not differ by genotype (Figure 4E: genotype: ($F_{(1, 10)} = 2.85$, $p = 0.09$), hemisphere: ($F_{(1, 10)} = 6.38$, $p = 0.052$). RD was strikingly higher in *Nrxn2α* KO mice (Figure 4F: genotype: ($F_{(1, 10)} = 26.06$, $p = 0.023$, power = 99.5%)), indicative of a change in demyelination, axonal density or orientation (54).

CLARITY reveals fibre disruption in *Nrxn2α* KO mice in the amygdala, orbitofrontal cortex, and anterior cingulate cortex

To further explore the differences as revealed by DTI, we performed CLARITY on the same brain tissue used in DTI, and stained with neurofilament and DAPI to label axons and cell bodies, respectively. We were then able to derive both the axonal alignment (as in, the geometric alignment of axons (from linear alignment to random) within 3D space (see Supp. Figure 2)) and density of the stained fibers, in addition to the cell density.

The pattern of results was broadly similar for both the prefrontal cortical ROIs. That is, first, axonal alignment was increased in *Nrxn2α* KO mice in the ACC

(Figure 5D: genotype: ($F_{(1, 10)}$ = 16.06, p = 0.011, power = 94.9%) but not the OFC (Figure 5G: genotype: ($F_{(1, 10)}$ = 5.56, p = 0.059). Second, this could not be explained by a difference in cell density, since that was similar between the KO and wild-type mice in both the ACC (Figure 5F: genotype: ($F_{(1, 10)}$ <1), hemisphere: ($F_{(1, 10)}$ = 1.73, p = 0.11) and the OFC (Figure 5H: genotype: ($F_{(1, 10)}$ = 3.09, p = 0.08). An increase in axonal density in *Nrxn2α* KO mice was reliable in the ACC (Figure 5E: genotype: ($F_{(1, 10)}$ = 14.64, p = 0.014, power = 93.0%), but not in the OFC (Figure 5H: genotype: ($F_{(1, 10)}$ = 3.09, p = 0.083).

We further examined two regions of the anterior amygdala, the BLA and basomedial (BMA) nuclei, where altered social cellular responses have been reported in human autism (38). We did not observe any significant differences for axonal alignment or fibre density in the BLA (see Supp. Figure 12A-C), but whereas axonal alignment (Figure 5J, genotype: $F_{(1, 10)}$ = 7.70, p = 0.045, power = 70.6%) but not axonal density (Figure 5K: genotype: ($F_{(1, 10)}$ = 6.10, p = 0.054) was increased in *Nrxn2α* KO mice in the basomedial nuclei, while cell density was unaffected (Figure 5L: genotype: ($F_{(1, 10)}$ <1). Alterations in axonal alignment and density as directly revealed by CLARITY could explain the increases in diffusivity and RD in the prefrontal regions, as measured by DTI.

To test the specificity of these alterations, we examined three further brain regions; the primary motor cortex (M1; Supp. Figure 12D-F), the primary somatosensory cortex (S1; Supp. Figure 12H-J) and the barrel field (BF; Supp. Figure 12K-M). Interestingly, although there were differences between

453 the hemispheres, there were no statistical differences between the genotypes
454 or genotype x hemisphere interactions for any measure (Supp. Table 3),
455 suggesting some specificity of the alterations in social-relevant brain regions
456 in *Nrxn2α* KO mice.
457
458 In summary, in both the prefrontal ROIs, namely the OFC, and the ACC, DTI
459 showed that ADC and RD were increased in *Nrxn2α* KO mice, likely related to
460 complementary analysis from CLARITY showing that axonal alignment was
461 altered in *Nrxn2α* KO mice in both prefrontal ROIs.
462
463 **Discussion**
464 Interestingly, the single-gene deletion of *Nrxn2α* captures several key aspects
465 of human ASD. In terms of behaviour, three studies have now found social
466 deficits associated with *Nrxn2α* KO (17-19); in terms of brain structure, as
467 reported here (summarised below), the *Nrxn2α* KO mouse model shows
468 altered microstructure and structural connectivity patterns in socially-relevant
469 brain regions reminiscent of changes in ASD.
470
471 A DTI approach has been used for some time to explore neuropathological
472 markers in autistic patients; alterations in myelination, axonal abundance, size
473 and orientation all modify FA and ADC values (21, 63), specifically by
474 reducing amygdala FA (23, 63), and have been used as a quantitative
475 measure of changes to brain white matter integrity (23, 24). Increased cortical
476 ADC typically indexes reduced functionality: e.g. increased hippocampal ADC
477 is associated with mild cognitive impairment (64, 65) and predicts verbal and

visuospatial memory in old healthy controls (66). Furthermore, both increased RD of various white matter tracts (67, 68) and increased whole-brain AD (68) have been observed in ASD. The *Nrxn2α* KO mouse reproduces many of these specific changes, including reduced FA and increases in ADC, AD and RD. Whole brain increases in ADC, AD and RD (but not FA) have been reported in ASD children, as have increases in ADC and RD in frontal cortex tracts (68). This is in agreement with other studies noting increased ADC in frontal cortex in ASD (63), as we observed here in both the prefrontal regions examined, the OFC and ACC. Likewise, FA was reduced in the amygdala in ASD children and adolescents (69), and right-sided lateralisation of abnormal amygdala/hippocampus-related connections, as seen in our *Nrxn2α* KO mouse, has been noted in high-functioning adolescents/adults with autism (70).

Whilst the current study specifically explores structural connectivity, it is difficult to extrapolate as to what these structural changes mean for functional connectivity in the *Nrxn2α* KO mouse. Hyper and hypo connectivity theories of autism have remained contentious, and vary in humans by cohort studied (e.g. by age of participant) (71). Further, in studies that have combined resting state functional MRI (rsfMRI) and DTI, functional and structural connectivity do not always overlap (72-74). Our current data suggests that DTI differences can be explained by altered axonal patterning (i.e. CLARITY). Others have explored the biological mechanisms linking structural connectivity to altered functional connectivity. Zhan et al. (2014) found that deletion of the chemokine receptor Cx3cr1 resulted in impaired synaptic pruning of long-

range connections during development, which manifested as impaired social behavior caused by decreased frontal functional connectivity, reduced synaptic multiplicity and weakened coherence of local field potentials (75). Thus, it is possible that impairments in neuronal structural maturation can generate functional connectivity deficits that encapsulate core autism phenotypes.

Our findings corroborate these quantifications of clinical autism, but highlights the question of what do the different measures of ADC, FA, AD and RD represent? Importantly, we observed these microstructural changes in various socially-relevant brain regions against a background of unchanged cell density in all our study's ROIs. Unexpectedly, this highlights the power of our new approach. Dudanova et al. (2007) concluded from measures of cell counting and cortical cell layer thickness that NRXN2 played little role in normal brain development (20). Indeed, in earlier studies, it was suggested that deletion of all *Nrxns* was unlikely to affect synaptic development but instead disrupts synaptic function (76). We propose that measures such as two-dimensional cell counting may be underestimating the impact of genetic mutations upon normal development. By staining cleared brain tissue with a nuclear marker and performing automated three-dimensional cell counting, we found no effect of *Nrxn2α* deletion on cell density in any region of interest examined. But this belies the clear effects upon microstructure integrity across multiple regions as measured by both DTI and CLARITY, and its specificity; only the socially-relevant brain regions we tested were disrupted, and not primary sensory or motor regions. Future studies will benefit from employing

more sensitive measures of brain structural connectivity to determine the relevance of genetic mutations in development.

FA and ADC can be influenced by changes in axonal density and alignment (e.g. by myelination, demyelination, axonal damage, loss of white matter coherence (77)). It is likely that the axonal alignment metric used to quantify CLARITY more closely reflects the ADC measure of DTI, given that ADC (or mean diffusivity) equally weights diffusion across all eigenvectors and does not bias the primary eigenvector as FA does. Thus, it is likely that alterations in the properties of axons in *Nrxn2α* KO mice are driving these changes in FA and ADC. Given we mostly see differences in RD, thought to reflect tract branching and myelination (as it measures λ_2 and λ_3), it is possible that the orientation in the perpendicular not parallel orientation of fibres is mostly affected. Given the differences in the amygdala, OFC and ACC, it is possible that even though neuronal densities are similar in the *Nrxn2α* KO brain, it is the connections between neurones and brain regions that are perturbed. This would be consistent with the idea that structural connectivity disruption may represent a core feature of autism (78). A broader question is how does the loss of *Nrxn2α* account for changes in axonal organisation? Ultimately, this question requires further studies. Others have shown that in *Nrxn2α* KO mice, excitatory transmitter release is reduced, as is short-term plasticity (18). Reduced glutamatergic release, even at a relatively long range to the synapse, can change the complexity of dendritic arbors (79). As this is a gene deletion model, it is conceivable that altered glutamatergic signalling during early development impairs appropriate synapse maturation, leading to the

553 structural changes we see herein. Further, how or whether these structural
554 changes fully explain the social impairments of *Nrxn2α* KO mice would require
555 new studies. Conceivably, inducible knock-down of *Nrxn2* (by inducible
556 knockout, siRNA, optogenetics etc.) within a specific brain region would
557 provide evidence that social abnormalities are being driven by *Nrxn2* loss.
558 However, developmentally-dependent altered structural connectivity would be
559 harder to definitively manipulate to explain changes in social behaviours.
560
561 Here we have developed a new application of CLARITY to quantitatively
562 investigate disease models by combining DTI with high resolution 3D imaging
563 and automated analysis of axonal fibres in a within subject study. Inevitably,
564 there are some technical limitations that will require future refinement as this
565 technology matures.
566
567 First, while we used CLARITY and immunolabeling to identify axons, we
568 cannot know whether axon-related changes alone reflect all the changes we
569 observed for our DTI measures. Second, whilst we can segment entire brain
570 regions for DTI analysis, it was not practical to image larger brain areas at the
571 necessary resolution for CLARITY. While it is theoretically possible that we
572 may bias sampling of each brain region by picking ROIs for multiphoton
573 imaging, this was done using atlas-defined coordinates and by an
574 experimenter blind to the DTI results, so minimising any bias. However, within
575 the current study, we were only able to apply the CLARITY approach to the
576 amygdala, OFC and ACC. It was not practical to apply this methodology to the
577 hippocampus, due to its extremely heterogeneous structure. The small cubic

ROIs could not be reproducibly positioned, and larger ROIs to average across larger areas of the hippocampus were not possible. Although imaging of fibre tracts in large volumes of cleared tissue is possible (80), fluorescent labelling limitations make it impractical for a study of this nature. Despite this, as the adoption of the CLARITY technique increases, we hope that the use of DTI and CLARITY to study structural connectivity across spatial scales will become commonplace.

As yet, no one DTI protocol has emerged as the standard for *in vivo* or *ex vivo* imaging. Indeed, there has been debate regarding the best number of diffusion gradients to use, among other parameters (81). Whilst some claim a minimum of 30 directions are required to estimate anisotropy (81), others claim that the benefits of using more than six are limited (82-85). A limitation of these studies is that these competing claims have not been complemented with standard neuroanatomical techniques. Where we found DTI differences, these were corroborated by the quantification of CLARITY (OFC, ACC, with BLA differences not reaching statistical significance after multiple-comparison correction). A further potential limitation of the current study is that groups of six animals may be underpowered. We argue for our approach here as follows. First, low variance in the datasets permits smaller group sizes. Second, for 18 of our 22 significant results, the observed power was more than 80%. Third, given the technical complexity of this approach, particularly in its early adoption and refinement stages, large sample throughput of multiple brain regions is challenging.

603 In summary, our combined use of DTI and CLARITY has revealed changes in
604 microstructure and structural connectivity of socially-relevant brain regions in
605 *Nrxn2α* KO mice that may underlie their deficits in social behaviour. It is hard
606 to conceive how these changes could have been observed using classical
607 experimental approaches. We envisage this approach will deliver a new level
608 of detail in structural connectivity approaches to understanding autism.
609

610 **Abbreviations**

611 ACC: anterior cingulate cortex
612 AD: axial diffusivity
613 ADC: apparent diffusion coefficient
614 ASD: autism spectrum disorder
615 BLA: basolateral amygdala
616 CLARITY: optically cleared brain tissue
617 DTI: diffusion tensor imaging
618 FA: fractional anisotropy
619 OFC: orbitofrontal cortex
620 Nrxn2: neurexin II
621 RD: radial diffusivity
622 ROI: region of interest
623

624 **Declarations**

625 **Ethics approval and consent to participate**

626 All experiments were performed under UK Home Office Project and Personal
627 Licenses in accordance with the Animals (Scientific Procedures) Act 1986,

628 and with the approval of the University of Leeds and Durham University
629 Animal Ethical and Welfare Review Boards.
630
631 **Consent for publication**
632 Not applicable
633
634 **Availability of data and material**
635 The codes used to quantify the CLARITY datasets are made available by
636 author LCA by email request to authors LCA or JD, subject to reference to the
637 current paper. The datasets used and/or analysed during the current study
638 are available from the corresponding author on reasonable request.
639
640 **Competing interests**
641 The authors declare no competing interests.
642
643 **Funding**
644 This work was supported by the Guy's and St. Thomas' Charity Prize PhD
645 scholarship to ALT, a Medical Research Council (UK) grant (G0900625) to
646 SJC and RJR, a University of Leeds Wellcome Trust ISSF (UK) Fellowship, a
647 Royal Society (UK) grant (RG130316), an Alzheimer's Society Fellowship
648 (AS-JF-15-008) to JD, a British Pharmacological Society (UK) grant to JD and
649 CL, a BBSRC grant to LCA (BB/P000479/1) and a BBSRC grant to CL
650 (BB/M008975/1). We acknowledge financial support from the Innovative
651 Medicines Initiative Joint Undertaking under grant agreement no. 115300,
652 resources of which are composed of financial contribution from the European

Union's Seventh Framework Programme (FP7/2007–2013) and EFPIA companies' in kind contribution, the Mortimer D Sackler Foundation and the Sackler Institute for Translational Neurodevelopment (ALT and LCA). Some analysis scripts were provided to ALT at the Computational Image Analysis in Cellular and Developmental Biology course at the Marine Biological Laboratory (Woods Hole, MA, USA), funded by National Institutes of Health (R25 GM103792-01).

Authors' contribution

EP, ALT, LCA and JD conceived the study. EP and ALT performed the experiments. EP, ALT, LCA and JD analysed the data. SJC, RJR, LCA and JD funded the study. All authors contributed to writing the paper. All authors have read and approved the final manuscript.

Acknowledgements

Not applicable.

References

1. Sandin S, Lichtenstein P, Kuja-Halkola R, Larsson H, Hultman CM, Reichenberg A. The familial risk of autism. Jama. 2014;311(17):1770-7.
2. Cardno AG, Gottesman, II. Twin studies of schizophrenia: from bow-and-arrow concordances to star wars Mx and functional genomics. American journal of medical genetics. 2000;97(1):12-7.
3. Ronald A, Happe F, Bolton P, Butcher LM, Price TS, Wheelwright S, et al. Genetic heterogeneity between the three components of the autism spectrum: a twin study. Journal of the American Academy of Child and Adolescent Psychiatry. 2006;45(6):691-9.
4. Ronemus M, Iossifov I, Levy D, Wigler M. The role of de novo mutations in the genetics of autism spectrum disorders. Nature reviews Genetics. 2014;15(2):133-41.
5. Geschwind DH, State MW. Gene hunting in autism spectrum disorder: on the path to precision medicine. The Lancet Neurology. 2015;14(11):1109-20.

685 6. Sahin M, Sur M. Genes, circuits, and precision therapies for autism and
686 related neurodevelopmental disorders. Science. 2015;350(6263).
687 7. Lise MF, El-Husseini A. The neuroligin and neurexin families: from structure
688 to function at the synapse. Cellular and molecular life sciences : CMLS.
689 2006;63(16):1833-49.
690 8. Sudhof TC. Synaptic Neurexin Complexes: A Molecular Code for the Logic
691 of Neural Circuits. Cell. 2017;171(4):745-69.
692 9. Gauthier J, Siddiqui TJ, Huashan P, Yokomaku D, Hamdan FF, Champagne
693 N, et al. Truncating mutations in NRXN2 and NRXN1 in autism spectrum disorders
694 and schizophrenia. Human genetics. 2011;130(4):563-73.
695 10. Mohrmann I, Gillessen-Kaesbach G, Siebert R, Caliebe A, Hellenbroich Y. A
696 de novo 0.57 Mb microdeletion in chromosome 11q13.1 in a patient with speech
697 problems, autistic traits, dysmorphic features and multiple endocrine neoplasia type 1.
698 European journal of medical genetics. 2011;54(4):e461-4.
699 11. Boyle MI, Jespersgaard C, Nazaryan L, Ravn K, Brondum-Nielsen K,
700 Bisgaard AM, et al. Deletion of 11q12.3-11q13.1 in a patient with intellectual
701 disability and childhood facial features resembling Cornelia de Lange syndrome.
702 Gene. 2015;572(1):130-4.
703 12. Li J, Wang L, Gou H, Shi L, Zhang K, Tang M, et al. Targeted sequencing and
704 functional analysis reveal brain-size-related genes and their networks in autism
705 spectrum disorders. Molecular Psychiatry. 2017;22:1282–90.
706 13. Yuan H, Li X, Wang Q, Yang W, Song J, Hu X, et al. A de novo 921Kb
707 microdeletion at 11q13.1 including neurexin 2 in a boy with developmental delay,
708 deficits in speech and language without autistic behaviors. European journal of
709 medical genetics. 2018.
710 14. Williams SM, An JY, Edson J, Watts M, Murigneux V, Whitehouse AJO, et
711 al. An integrative analysis of non-coding regulatory DNA variations associated with
712 autism spectrum disorder. Molecular psychiatry. 2018.
713 15. Wang J, Gong J, Li L, Chen Y, Liu L, Gu H, et al. Neurexin gene family
714 variants as risk factors for autism spectrum disorder. Autism research : official journal
715 of the International Society for Autism Research. 2018;11(1):37-43.
716 16. Duda M, Zhang H, Li HD, Wall DP, Burmeister M, Guan Y. Brain-specific
717 functional relationship networks inform autism spectrum disorder gene prediction.
718 Translational psychiatry. 2018;8(1):56.
719 17. Dachtler J, Glasper J, Cohen RN, Ivorra JL, Swiffen DJ, Jackson AJ, et al.
720 Deletion of alpha-neurexin II results in autism-related behaviors in mice.
721 Translational psychiatry. 2014;4:e484.
722 18. Born G, Grayton HM, Langhorst H, Dudanova I, Rohlmann A, Woodward
723 BW, et al. Genetic targeting of NRXN2 in mice unveils role in excitatory cortical
724 synapse function and social behaviors. Frontiers in synaptic neuroscience. 2015;7:3.
725 19. Dachtler J, Ivorra JL, Rowland TE, Lever C, Rodgers RJ, Clapcote SJ.
726 Heterozygous deletion of alpha-neurexin I or alpha-neurexin II results in behaviors
727 relevant to autism and schizophrenia. Behavioral neuroscience. 2015;129(6):765-76.
728 20. Dudanova I, Tabuchi K, Rohlmann A, Sudhof TC, Missler M. Deletion of
729 alpha-neurexins does not cause a major impairment of axonal pathfinding or synapse
730 formation. The Journal of comparative neurology. 2007;502(2):261-74.
731 21. Beaulieu C. The basis of anisotropic water diffusion in the nervous system - a
732 technical review. NMR in biomedicine. 2002;15(7-8):435-55.

733 22. Barnea-Goraly N, Kwon H, Menon V, Eliez S, Lotspeich L, Reiss AL. White
734 matter structure in autism: preliminary evidence from diffusion tensor imaging.
735 Biological psychiatry. 2004;55(3):323-6.
736 23. Noriuchi M, Kikuchi Y, Yoshiura T, Kira R, Shigeto H, Hara T, et al. Altered
737 white matter fractional anisotropy and social impairment in children with autism
738 spectrum disorder. Brain research. 2010;1362:141-9.
739 24. Belmonte MK, Allen G, Beckel-Mitchener A, Boulanger LM, Carper RA,
740 Webb SJ. Autism and abnormal development of brain connectivity. The Journal of
741 neuroscience : the official journal of the Society for Neuroscience. 2004;24(42):9228-
742 31.
743 25. Chung K, Wallace J, Kim SY, Kalyanasundaram S, Andalman AS, Davidson
744 TJ, et al. Structural and molecular interrogation of intact biological systems. Nature.
745 2013;497(7449):332-7.
746 26. Pervolaraki E, Anderson RA, Benson AP, Hayes-Gill B, Holden AV, Moore
747 BJ, et al. Antenatal architecture and activity of the human heart. Interface focus.
748 2013;3(2):20120065.
749 27. Paxinos G, Franklin K. The Mouse Brain in Stereotaxic Coordinates. Third ed:
750 Academic Press; 2008.
751 28. Pervolaraki E, Dachtler J, Anderson RA, Holden AV. Ventricular myocardium
752 development and the role of connexins in the human fetal heart. Scientific reports.
753 2017;7(1):12272.
754 29. Yeh FC, Verstynen TD, Wang Y, Fernandez-Miranda JC, Tseng WY.
755 Deterministic diffusion fiber tracking improved by quantitative anisotropy. PloS one.
756 2013;8(11):e80713.
757 30. Basser PJ, Mattiello J, LeBihan D. Estimation of the effective self-diffusion
758 tensor from the NMR spin echo. Journal of magnetic resonance Series B.
759 1994;103(3):247-54.
760 31. Jiang H, van Zijl PC, Kim J, Pearlson GD, Mori S. DtiStudio: resource
761 program for diffusion tensor computation and fiber bundle tracking. Computer
762 methods and programs in biomedicine. 2006;81(2):106-16.
763 32. Ferguson JN, Aldag JM, Insel TR, Young LJ. Oxytocin in the medial
764 amygdala is essential for social recognition in the mouse. The Journal of neuroscience
765 : the official journal of the Society for Neuroscience. 2001;21(20):8278-85.
766 33. Tanimizu T, Kenney JW, Okano E, Kadoma K, Frankland PW, Kida S.
767 Functional Connectivity of Multiple Brain Regions Required for the Consolidation of
768 Social Recognition Memory. The Journal of neuroscience : the official journal of the
769 Society for Neuroscience. 2017;37(15):4103-16.
770 34. Emery NJ, Capitanio JP, Mason WA, Machado CJ, Mendoza SP, Amaral DG.
771 The effects of bilateral lesions of the amygdala on dyadic social interactions in rhesus
772 monkeys (Macaca mulatta). Behavioral neuroscience. 2001;115(3):515-44.
773 35. Rosvold HE, Mirsky AF, Pribram KH. Influence of amygdalectomy on social
774 behavior in monkeys. Journal of comparative and physiological psychology.
775 1954;47(3):173-8.
776 36. Mosher CP, Zimmerman PE, Gothard KM. Neurons in the monkey amygdala
777 detect eye contact during naturalistic social interactions. Current biology : CB.
778 2014;24(20):2459-64.
779 37. Rutishauser U, Mamelak AN, Adolphs R. The primate amygdala in social
780 perception - insights from electrophysiological recordings and stimulation. Trends in
781 neurosciences. 2015;38(5):295-306.

782 38. Rutishauser U, Tudusciuc O, Wang S, Mamelak AN, Ross IB, Adolphs R.
783 Single-neuron correlates of atypical face processing in autism. Neuron.
784 2013;80(4):887-99.
785 39. Adolphs R, Tranel D, Damasio AR. The human amygdala in social judgment.
786 Nature. 1998;393(6684):470-4.
787 40. Baron-Cohen S, Ring HA, Bullmore ET, Wheelwright S, Ashwin C, Williams
788 SC. The amygdala theory of autism. Neuroscience and biobehavioral reviews.
789 2000;24(3):355-64.
790 41. Maaswinkel H, Baars AM, Gispen WH, Spruijt BM. Roles of the basolateral
791 amygdala and hippocampus in social recognition in rats. Physiology & behavior.
792 1996;60(1):55-63.
793 42. Kogan JH, Frankland PW, Silva AJ. Long-term memory underlying
794 hippocampus-dependent social recognition in mice. Hippocampus. 2000;10(1):47-56.
795 43. Okuyama T, Kitamura T, Roy DS, Itohara S, Tonegawa S. Ventral CA1
796 neurons store social memory. Science. 2016;353(6307):1536-41.
797 44. van der Kooij MA, Fantin M, Kraev I, Korshunova I, Grosse J, Zanoletti O, et
798 al. Impaired hippocampal neuroligin-2 function by chronic stress or synthetic peptide
799 treatment is linked to social deficits and increased aggression.
800 Neuropsychopharmacology : official publication of the American College of
801 Neuropsychopharmacology. 2014;39(5):1148-58.
802 45. Rubin RD, Watson PD, Duff MC, Cohen NJ. The role of the hippocampus in
803 flexible cognition and social behavior. Frontiers in human neuroscience. 2014;8:742.
804 46. Nicolson R, DeVito TJ, Vidal CN, Sui Y, Hayashi KM, Drost DJ, et al.
805 Detection and mapping of hippocampal abnormalities in autism. Psychiatry research.
806 2006;148(1):11-21.
807 47. Schumann CM, Hamstra J, Goodlin-Jones BL, Lotspeich LJ, Kwon H,
808 Buonocore MH, et al. The amygdala is enlarged in children but not adolescents with
809 autism; the hippocampus is enlarged at all ages. The Journal of neuroscience : the
810 official journal of the Society for Neuroscience. 2004;24(28):6392-401.
811 48. Bachevalier J, Loveland KA. The orbitofrontal-amygdala circuit and self-
812 regulation of social-emotional behavior in autism. Neuroscience and biobehavioral
813 reviews. 2006;30(1):97-117.
814 49. Beer JS, John OP, Scabini D, Knight RT. Orbitofrontal cortex and social
815 behavior: integrating self-monitoring and emotion-cognition interactions. Journal of
816 cognitive neuroscience. 2006;18(6):871-9.
817 50. Watson KK, Platt ML. Social signals in primate orbitofrontal cortex. Current
818 biology : CB. 2012;22(23):2268-73.
819 51. Girgis RR, Minshew NJ, Melhem NM, Nutche JJ, Keshavan MS, Hardan AY.
820 Volumetric alterations of the orbitofrontal cortex in autism. Progress in neuro-
821 psychopharmacology & biological psychiatry. 2007;31(1):41-5.
822 52. Tyson AL, Hilton ST, Andreae LC. Rapid, simple and inexpensive production
823 of custom 3D printed equipment for large-volume fluorescence microscopy.
824 International journal of pharmaceutics. 2015;494(2):651-6.
825 53. Herbert MR, Ziegler DA, Deutsch CK, O'Brien LM, Kennedy DN, Filipek
826 PA, et al. Brain asymmetries in autism and developmental language disorder: a nested
827 whole-brain analysis. Brain : a journal of neurology. 2005;128(Pt 1):213-26.
828 54. Alexander AL, Lee JE, Lazar M, Field AS. Diffusion tensor imaging of the
829 brain. Neurotherapeutics : the journal of the American Society for Experimental
830 NeuroTherapeutics. 2007;4(3):316-29.

831 55. Alexander AL, Lee JE, Lazar M, Boudos R, DuBray MB, Oakes TR, et al.
832 Diffusion tensor imaging of the corpus callosum in Autism. NeuroImage.
833 2007;34(1):61-73.
834 56. Travers BG, Tromp do PM, Adluru N, Lange N, Destiche D, Ennis C, et al.
835 Atypical development of white matter microstructure of the corpus callosum in males
836 with autism: a longitudinal investigation. Molecular autism. 2015;6:15.
837 57. Ellegood J, Babineau BA, Henkelman RM, Lerch JP, Crawley JN.
838 Neuroanatomical analysis of the BTBR mouse model of autism using magnetic
839 resonance imaging and diffusion tensor imaging. NeuroImage. 2013;70:288-300.
840 58. Kumar M, Kim S, Pickup S, Chen R, Fairless AH, Ittyerah R, et al.
841 Longitudinal in-vivo diffusion tensor imaging for assessing brain developmental
842 changes in BALB/cJ mice, a model of reduced sociability relevant to autism. Brain
843 research. 2012;1455:56-67.
844 59. Pitkanen A, Pikkarainen M, Nurminen N, Ylinen A. Reciprocal connections
845 between the amygdala and the hippocampal formation, perirhinal cortex, and
846 postrhinal cortex in rat. A review. Annals of the New York Academy of Sciences.
847 2000;911:369-91.
848 60. Cavada C, Company T, Tejedor J, Cruz-Rizzolo RJ, Reinoso-Suarez F. The
849 anatomical connections of the macaque monkey orbitofrontal cortex. A review.
850 Cerebral cortex. 2000;10(3):220-42.
851 61. Abrams DA, Lynch CJ, Cheng KM, Phillips J, Supekar K, Ryali S, et al.
852 Underconnectivity between voice-selective cortex and reward circuitry in children
853 with autism. Proceedings of the National Academy of Sciences of the United States of
854 America. 2013;110(29):12060-5.
855 62. Murphy ER, Foss-Feig J, Kenworthy L, Gaillard WD, Vaidya CJ. Atypical
856 Functional Connectivity of the Amygdala in Childhood Autism Spectrum Disorders
857 during Spontaneous Attention to Eye-Gaze. Autism research and treatment.
858 2012;2012:652408.
859 63. Sundaram SK, Kumar A, Makki MI, Behen ME, Chugani HT, Chugani DC.
860 Diffusion tensor imaging of frontal lobe in autism spectrum disorder. Cerebral cortex.
861 2008;18(11):2659-65.
862 64. Fellgiebel A, Wille P, Muller MJ, Winterer G, Scheurich A, Vucurevic G, et
863 al. Ultrastructural hippocampal and white matter alterations in mild cognitive
864 impairment: a diffusion tensor imaging study. Dementia and geriatric cognitive
865 disorders. 2004;18(1):101-8.
866 65. Stebbins GT, Murphy CM. Diffusion tensor imaging in Alzheimer's disease
867 and mild cognitive impairment. Behavioural neurology. 2009;21(1):39-49.
868 66. Carlesimo GA, Cherubini A, Caltagirone C, Spalletta G. Hippocampal mean
869 diffusivity and memory in healthy elderly individuals: a cross-sectional study.
870 Neurology. 2010;74(3):194-200.
871 67. Ameis SH, Fan J, Rockel C, Voineskos AN, Lobaugh NJ, Soorya L, et al.
872 Impaired structural connectivity of socio-emotional circuits in autism spectrum
873 disorders: a diffusion tensor imaging study. PloS one. 2011;6(11):e28044.
874 68. Shukla DK, Keehn B, Muller RA. Tract-specific analyses of diffusion tensor
875 imaging show widespread white matter compromise in autism spectrum disorder.
876 Journal of child psychology and psychiatry, and allied disciplines. 2011;52(3):286-95.
877 69. Jou RJ, Jackowski AP, Papademetris X, Rajeevan N, Staib LH, Volkmar FR.
878 Diffusion tensor imaging in autism spectrum disorders: preliminary evidence of
879 abnormal neural connectivity. The Australian and New Zealand journal of psychiatry.
880 2011;45(2):153-62.

881 70. Conturo TE, Williams DL, Smith CD, Gultepe E, Akbudak E, Minshew NJ.
882 Neuronal fiber pathway abnormalities in autism: an initial MRI diffusion tensor
883 tracking study of hippocampo-fusiform and amygdalo-fusiform pathways. Journal of
884 the International Neuropsychological Society : JINS. 2008;14(6):933-46.
885 71. Stanfield AC, McIntosh AM, Spencer MD, Philip R, Gaur S, Lawrie SM.
886 Towards a neuroanatomy of autism: a systematic review and meta-analysis of
887 structural magnetic resonance imaging studies. European psychiatry : the journal of
888 the Association of European Psychiatrists. 2008;23(4):289-99.
889 72. Vissers ME, Cohen MX, Geurts HM. Brain connectivity and high functioning
890 autism: a promising path of research that needs refined models, methodological
891 convergence, and stronger behavioral links. Neuroscience and biobehavioral reviews.
892 2012;36(1):604-25.
893 73. Rudie JD, Brown JA, Beck-Pancer D, Hernandez LM, Dennis EL, Thompson
894 PM, et al. Altered functional and structural brain network organization in autism.
895 NeuroImage Clinical. 2012;2:79-94.
896 74. Uddin LQ, Supekar K, Menon V. Reconceptualizing functional brain
897 connectivity in autism from a developmental perspective. Frontiers in human
898 neuroscience. 2013;7:458.
899 75. Zhan Y, Paolicelli RC, Sforazzini F, Weinhard L, Bolasco G, Pagani F, et al.
900 Deficient neuron-microglia signaling results in impaired functional brain connectivity
901 and social behavior. Nature neuroscience. 2014;17(3):400-6.
902 76. Missler M, Zhang W, Rohlmann A, Kattenstroth G, Hammer RE, Gottmann
903 K, et al. Alpha-neurexins couple Ca2+ channels to synaptic vesicle exocytosis.
904 Nature. 2003;423(6943):939-48.
905 77. Alba-Ferrara LM, de Erausquin GA. What does anisotropy measure? Insights
906 from increased and decreased anisotropy in selective fiber tracts in schizophrenia.
907 Frontiers in integrative neuroscience. 2013;7:9.
908 78. Minshew NJ, Williams DL. The new neurobiology of autism: cortex,
909 connectivity, and neuronal organization. Archives of neurology. 2007;64(7):945-50.
910 79. Andreae LC, Burrone J. Spontaneous Neurotransmitter Release Shapes
911 Dendritic Arbors via Long-Range Activation of NMDA Receptors. Cell reports. 2015.
912 80. Ye L, Allen WE, Thompson KR, Tian Q, Hsueh B, Ramakrishnan C, et al.
913 Wiring and Molecular Features of Prefrontal Ensembles Representing Distinct
914 Experiences. Cell. 2016;165(7):1776-88.
915 81. Jones DK. The effect of gradient sampling schemes on measures derived from
916 diffusion tensor MRI: a Monte Carlo study. Magnetic resonance in medicine.
917 2004;51(4):807-15.
918 82. Lebel C, Benner T, Beaulieu C. Six is enough? Comparison of diffusion
919 parameters measured using six or more diffusion-encoding gradient directions with
920 deterministic tractography. Magnetic resonance in medicine. 2012;68(2):474-83.
921 83. Hasan KM, Parker DL, Alexander AL. Comparison of gradient encoding
922 schemes for diffusion-tensor MRI. Journal of magnetic resonance imaging : JMRI.
923 2001;13(5):769-80.
924 84. Yao X, Yu T, Liang B, Xia T, Huang Q, Zhuang S. Effect of increasing
925 diffusion gradient direction number on diffusion tensor imaging fiber tracking in the
926 human brain. Korean journal of radiology. 2015;16(2):410-8.
927 85. Ni H, Kavcic V, Zhu T, Ekholm S, Zhong J. Effects of number of diffusion
928 gradient directions on derived diffusion tensor imaging indices in human brain. AJNR
929 American journal of neuroradiology. 2006;27(8):1776-81.
930

Figure Legends

Figure 1

Quantification of CLARITY imaging. **A** Sections of DTI-scanned brain were segmented at different Bregma levels for (i) the orbitofrontal cortex, (ii) the anterior hippocampus and amygdala, (iii) the mid hippocampus and posterior amygdala and (iv) the posterior hippocampus. **B-D** DTI-scanned brains were computed for tracts. Tissue from wild-type and *Nrxn2α* KO mice were cleared and stained for neurofilament and DAPI (**E**). **F** Automated MATLAB scripts were used to segment the DAPI (blue) and neurofilament (purple) channels such that cell density and axonal density and orientation could be calculated. **G** is representative of a CLARITY-derived 3D stacked image of a DAPI and neurofilament of a region of interest, with **H** being the corresponding segmented image. Scale bar: 100 μm.

Figure 2

Deletion of *Nrxn2α* reduces amygdala fractional anisotropy (FA) but not apparent diffusion coefficient (ADC). DTI images of the amygdala was segmented at two regions; anterior (Bregma -1.94 mm) and posterior (Bregma -2.46 mm). FA of the whole amygdala structure was significantly reduced in the posterior (**B**) but not (**A**) region. FA was also significantly reduced in the anterior basolateral amygdala (BLA) (**C**). However, ADC was similar between the genotypes in the anterior (**D**), posterior (**E**) and BLA (**F**). **=P<0.01, *=P<0.05. Error bars represent s.e.m. Wild-type n=6, *Nrxn2α* KO n=6.

Figure 3

Nrxn2α KO mice have increased apparent diffusion coefficient (ADC) and axial (AD) and radial diffusivity (RD) in the orbitofrontal cortex (OFC) and the anterior cingulate cortex (ACC). Although reduced, there was no significant difference between wild-types and *Nrxn2α* KO mice for FA in the OFC (**A**) and ACC (**C**), but ADC was significantly increased in *Nrxn2α* KO mice in both prefrontal regions (**B** and **D**). The OFC has significantly increased AD and RD (**E-F**), whereas only RD was increased in the ACC (**G-H**). ***=P=0.0005, ***=P<0.001, **=P<0.01, *=P<0.05. Error bars represent s.e.m. Wild-type n=6, *Nrxn2α* KO n=6.

Figure 4

Tractographic analysis of amygdala-hippocampus and amygdala-orbitofrontal cortex (OFC) connectivity. Amygdala-hippocampal connections are characterised by greater right hemisphere axial diffusivity (AD) *Nrxn2α* KO mice (**A**) but not radial diffusivity (RD) (**B**). Specific to the BLA, connections to the anterior hippocampus (**C**) and posterior hippocampus (**D**) have greater right hemisphere AD. Although the amygdala-OFC connection was similar between the genotypes for AD (**E**), *Nrxn2α* KO mice had significantly increased RD (**F**). *=P<0.05, ***=P<0.001. Error bars represent s.e.m. Wild-type n=6, Nrxn2α KO n=6.

Figure 5

CLARITY reveals differences in axonal alignment and fibre density in *Nrxn2α* KO mice. (**A-C**) Representative images of the CLARITY-treated brain, with ROI defined for the anterior cingulate cortex (ACC), orbitofrontal cortex

(OFC), basomedial amygdala (BMA) and basolateral amygdala (BLA). For the ACC, the axonal alignment (**D**) and axon density (**E**) were significantly altered in KO mice, but cell density was unaltered (**F**). Within the medial OFC, only axonal alignment was significantly altered in KOs (**G**), with axon density (**H**) and cell density (**I**) being similar. For the BMA, both the axonal alignment (**J**) and axon density (**K**) were significantly increased, whilst cell density was unaltered (**L**). *=P<0.05, **=P<0.01. Error bars represent s.e.m. Wild-type n=6, *Nrxn2α* KO n=6.

The within-subject application of diffusion tensor MRI and CLARITY reveals brain structural changes in *Nrxn2* deletion mice

Supplemental Material

Eleftheria Pervolaraki Ph.D, Adam L. Tyson MRes, Francesca Pibiri Ph.D, Steven L. Poulter Ph.D, Amy C. Reichelt Ph.D, R. John Rodgers Ph.D, Steven J. Clapcote Ph.D, Colin Lever Ph.D, Laura C. Andreae M.D. Ph.D, James Dachtler Ph.D

Supplemental Materials and Methods

Diffusion Tensor MRI

Data Acquisition

Brain MR imaging was performed on a vertical 9.4 Tesla spectrometer (Bruker AVANCE II NMR, Ettlingen, Germany) with an 89 mm wide bore, 3 radio frequency channels with digital broadband frequency synthesis (6-620 MHz) and an imaging coil with diameter of 25 mm for hydrogen (1H). 3D images for each brain were obtained using a DT-MRI protocol (TE: 35 ms, TR: 700 ms, 10 signal averages). The field of view was set at 128 x 128 x 128, with a cubic resolution of 100 μm/pixel and a b value of 1200 s/mm^2. For each brain, diffusion weighted images were obtained in 6 directions, based upon recent published protocols (1-5). The subject of the number of diffusions gradients has been debated (6), with studies suggesting limited benefits of using more than 6 directions in biological tissue (7-9). The imaging time for each brain was 60 hours.

CLARITY

Solutions:

Hydrogel solution: 2% PFA 2% acrylamide 0.05% bis-acrylamide and 0.25% VA-044 thermal initiator (2,2'-Azobis[2-(2-imidazolin-2-yl) propane] dihydrochloride) in PBS, pH 7.4.

Clearing buffer: 8% Sodium dodecyl sulfate in 200mM boric acid, pH 8.5.

Multiphoton imaging – methodological outline

Cleared samples were mounted in custom 3D printed chambers for two-photon imaging. Images were acquired using ZEN Black (Zeiss, Germany). DAPI signal was detected using a 485 nm short pass filter, and neurofilament using a 500-550 nm band pass filter. The power of the excitation laser was varied to maximise the dynamic range for each image, but all other parameters were kept constant. The images were analysed using custom MATLAB (version 9.1, The Mathworks Inc.) scripts. Two-dimensional images were visualised using ImageJ (10) and three-dimensional images using Vaa3D (11).

Multiphoton imaging and analysis – image analysis method

Pre-processing

Image files were loaded into MATLAB (The Mathworks Ltd.) using the BioFormats toolbox (12), and the raw image data were obtained along with the precise voxel dimensions from the metadata. Each two-dimensional (2D) image from the three-dimensional (3D) stack was initially corrected for uneven background illumination by element-wise division by a 2D reference image. This reference image was calculated as the mean 2D image through the 3D stack, which was smoothed using a 2D Gaussian kernel with a full-width at half maximum (FWHM) of 20 % of the geometric mean of the dimensions of the 2D image (mean dimension). The image was denoised by filtering the image with a Gaussian kernel with a standard deviation of one pixel. Background subtraction was carried out by subtracting a smoothed, filtered image (FWHM 10 % of the mean dimension). Each pixel was then smoothed using a 3D Gaussian kernel with FWHM of 1.5 μm (the largest axonal diameter expected according to Perge et al. (13).

Segmentation

The numerical gradient of the image in each dimension $(\Delta X, \Delta Y, \Delta Z)$ was calculated, and these were combined to calculate the magnitude of the gradient $\left(\sqrt{\Delta X^2 + \Delta Y^2 + \Delta Z^2}\right)$. The resulting image was thresholded, using a combination of the Otsu (1979) and Rosin (2001) methods (Rosin threshold + 2/5 Otsu threshold) (14, 15). The gradient image highlights the edge of each axon; to combine these into a single object, the image was dilated and then eroded with a cubic structuring element (each side being 1.5 μm, to 'close' the largest axons as per Perge et al. (13)). Very small objects (less than 50 μm^3) were removed from the image as they reflected noise, very small neuronal processes and gradients around cells.

Owing to variations in staining intensity of different axons, the thresholding produced segmented axons of various thicknesses that did not necessarily reflect the true structure. To remove this bias, the thresholded image was skeletonised using a homotopic thinning algorithm (16) implemented in MATLAB(17). The resulting image was dilated and then eroded using a cubic structuring element (10 pixels on each side for dilation, 9 for erosion) to produce connected processes with a uniform two-pixel diameter. This dilation ensured that the voxels in the binary image were connected via their faces (6-connected) rather than just their corners (26-connected), which better reflects the true structure of biological processes. This method detects

most large axons at the expense of smaller processes, and the loss of any information about axon diameter. These steps are outlined in Supp. Figure 2.

Analysis

The density of axons was calculated as the fraction of the image volume taken up by the segmented axons. A measure of axonal alignment was calculated by determining the mean axonal alignment along each dimension. This alignment was calculated by moving along the 3D image in a single dimension, keeping the coordinates in the other dimensions constant, and counting the number of times the pixel intensity did not change (i.e. how many times an axon was not entered or left). This number was averaged across each face of the image volume and scaled to the length of each dimension to produce a metric of how constant the image intensity is in that dimension. The perfect case of no intensity change (i.e. all axons are aligned perfectly with a particular dimension) gives a value of 1. The greater the difference between this measure in each three dimensions, the more aligned the axons must be (i.e. their directions are anisotropic). The standard deviation of this measure across the three dimensions was calculated as the axonal alignment.

The alignment calculation is illustrated in Supp. Figure 3 for a simple, two-dimensional case. Supp. Figure 3a shows the case of low axonal alignment, and Supp. Figure 3b shows the case of high axonal alignment. In each case, for illustration, each pixel represented by a small square on the grid is classed as either containing an axon or not. In the real images, the pixels are smaller, and are actually binary. In each axis, the number of pixel transitions in which the presence of an axon does not change is divided by the number of transitions, and the average is calculated. The standard deviation of this average for all axes is the measure of axonal alignment. When the alignment is low, the two averages are similar, and the standard deviation is low. When the alignment is high the two averages are very different, and the standard deviation is high. To analyse the real data, this same calculation is carried out in 3D, but in a much larger grid of voxels. Cell density was calculated as the number of cells per mm^3.

Supp. Table 1

Brain Region	DTI Measure	ANOVA Comparison	F Value	P Value
Anterior Hippocampus	FA	Genotype	$F_{(1,10)} = 3.91$	P = 0.063
		Hemisphere	$F_{(1,10)} = 3.89$	P = 0.065
Mid Hippocampus	FA	Genotype	$F_{(1,10)} = 3.12$	P = 0.07
		Hemisphere	$F_{(1,10)} < 1$	P = 0.146
Posterior Hippocampus	FA	Genotype	$F_{(1,10)} = 1.99$	P = 0.104
		Hemisphere	$F_{(1,10)} = 1.95$	P = 0.101
Anterior Hippocampus	ADC	Genotype	$F_{(1,10)} = 3.17$	P = 0.073
		Hemisphere	$F_{(1,10)} = 2.20$	P = 0.095
Mid Hippocampus	ADC	Genotype	$F_{(1,10)} < 1$	P = 0.160
		Hemisphere	$F_{(1,10)} = 1.62$	P = 0.115
Posterior Hippocampus	ADC	**Genotype**	**$F_{(1,10)} = 8.88$**	**P = 0.036**
		Hemisphere	$F_{(1,10)} < 1$	P = 0.180
Anterior Hippocampus	AD	Genotype	$F_{(1,10)} < 1$	P = 0.187
		Hemisphere	$F_{(1,10)} = 1.07$	P = 0.121
Mid Hippocampus	AD	Genotype	$F_{(1,10)} < 1$	P = 0.153
		Hemisphere	$F_{(1,10)} = 1.04$	P = 0.124
Posterior Hippocampus	AD	Genotype	$F_{(1,10)} = 3.45$	P = 0.07
		Hemisphere	**$F_{(1,10)} = 6.19$**	P = 0.052
Anterior Hippocampus	RD	Genotype	$F_{(1,10)} = 3.03$	P = 0.086
		Hemisphere	$F_{(1,10)} < 1$	P = 0.137
Mid Hippocampus	RD	Genotype	$F_{(1,10)} < 1$	P = 0.140
		Hemisphere	$F_{(1,10)} = 1.33$	P = 0.119
Posterior Hippocampus	RD	**Genotype**	**$F_{(1,10)} = 10.83$**	**P = 0.027**
		Hemisphere	$F_{(1,10)} = 3.48$	P = 0.07

Statistical analysis of the anterior (Bregma -1.94 mm), mid (Bregma -2.46 mm) and posterior (Bregma -3.28 mm) hippocampus for fractional anisotropy (FA), apparent diffusion coefficient (ADC), axial diffusion (AD) and radial diffusion (RD). Analysis was performed using repeated measure two-way ANOVAs for genotype and hemisphere (Benjamini-Hochberg corrected (corrected P values stated)).

Supp. Table 2

Brain Region	DTI Measure	ANOVA Comparison	F Value	P Value
Amygdala-Anterior Hippocampus	AD	Genotype	$F_{(1,10)}$ <1	P = 0.164
		Hemisphere	$F_{(1,10)}$ = 2.10	P = 0.097
		Genotype x Hemisphere	**$F_{(1,10)}$ = 12.12**	**P = 0.023**
Amygdala-Anterior Hippocampus	RD	Genotype	$F_{(1,10)}$ <1	P = 0.149
		Hemisphere	$F_{(1,10)}$ = 1.32	P = 0.106
		Genotype x Hemisphere	$F_{(1,10)}$ <1	P = 0.155
Amygdala-Posterior Hippocampus	AD	Genotype	$F_{(1,10)}$ <1	P = 0.142
		Hemisphere	$F_{(1,10)}$ <1	P = 0.189
		Genotype x Hemisphere	$F_{(1,10)}$ = 4.54	P = 0.061
Amygdala-Posterior Hippocampus	RD	Genotype	$F_{(1,10)}$ <1	P = 0.151
		Hemisphere	$F_{(1,10)}$ <1	P = 0.135
		Genotype x Hemisphere	$F_{(1,10)}$ <1	P = 0.128
BLA-Anterior Hippocampus	AD	Genotype	$F_{(1,10)}$ <1	P = 0.167
		Hemisphere	**$F_{(1,10)}$ = 6.59**	**P = 0.047**
		Genotype x Hemisphere	**$F_{(1,10)}$ = 10.53**	**P = 0.032**
BLA-Anterior Hippocampus	RD	Genotype	$F_{(1,10)}$ <1	P = 0.158
		Hemisphere	$F_{(1,10)}$ = 2.59	P = 0.092
		Genotype x Hemisphere	$F_{(1,10)}$ <1	P = 0.173
BLA-Posterior Hippocampus	AD	Genotype	$F_{(1,10)}$ <1	P = 0.169
		Hemisphere	**$F_{(1,10)}$ = 12.79**	**P = 0.018**
		Genotype x Hemisphere	**$F_{(1,10)}$ = 12.97**	**P = 0.02**
BLA-Posterior Hippocampus	RD	Genotype	$F_{(1,10)}$ <1	P = 0.162
		Hemisphere	$F_{(1,10)}$ = 3.11	P = 0.077
		Genotype x Hemisphere	$F_{(1,10)}$ <1	P = 0.178

Statistical analysis of the anterior (Bregma -1.94 mm), and posterior (Bregma -3.28 mm) amygdala-hippocampal connections, analysed for axial diffusion (AD) and radial diffusion (RD). Analysis was performed using repeated measure two-way ANOVAs for genotype and hemisphere (Benjamini-Hochberg corrected (corrected P values stated)).

Supp. Table 3

Brain Region	CLARITY Measure	ANOVA Comparison	F Value	P Value
M1	OI	Genotype	$F_{(1,10)}$ <1	P = 0.182
		Hemisphere	$F_{(1,10)}$ = 1.74	P = 0.108
M1	Cell Density	Genotype	$F_{(1,10)}$ = 2.04	P = 0.099
		Hemisphere	$F_{(1,10)}$ = 1.41	P = 0.117
M1	Fibre Density	Genotype	$F_{(1,10)}$ <1	P = 0.171
		Hemisphere	$F_{(1,10)}$ <1	P = 0.176
S1	OI	Genotype	$F_{(1,10)}$ <1	P = 0.185
		Hemisphere	**$F_{(1,10)}$ = 36.86**	**P = 0.005**
S1	Cell Density	Genotype	$F_{(1,10)}$ <1	P = 0.131
		Hemisphere	**$F_{(1,10)}$ = 13.73**	**P = 0.016**
S1	Fibre Density	Genotype	$F_{(1,10)}$ = 1.73	P = 0.110
		Hemisphere	**$F_{(1,10)}$ = 8.51**	**P = 0.038**
BF	OI	Genotype	$F_{(1,10)}$ <1	P = 0.191
		Hemisphere	**$F_{(1,10)}$ = 10.59**	**P = 0.034**
BF	Cell Density	Genotype	$F_{(1,10)}$ <1	P = 0.133
		Hemisphere	**$F_{(1,10)}$ = 8.70**	**P = 0.041**
BF	Fibre Density	Genotype	$F_{(1,10)}$ <1	P = 0.144
		Hemisphere	$F_{(1,10)}$ <1	P = 0.126

Statistical analysis of the primary motor cortex (M1), primary somatosensory cortex (S1) and the barrel field (BF). CLARITY imaged regions were then analysed for orientation index (OI), cell density and fibre density. Analysis was performed using repeated measure two-way ANOVAs for genotype and hemisphere (Benjamini-Hochberg corrected (corrected P values stated)).

Supp. Figure 1

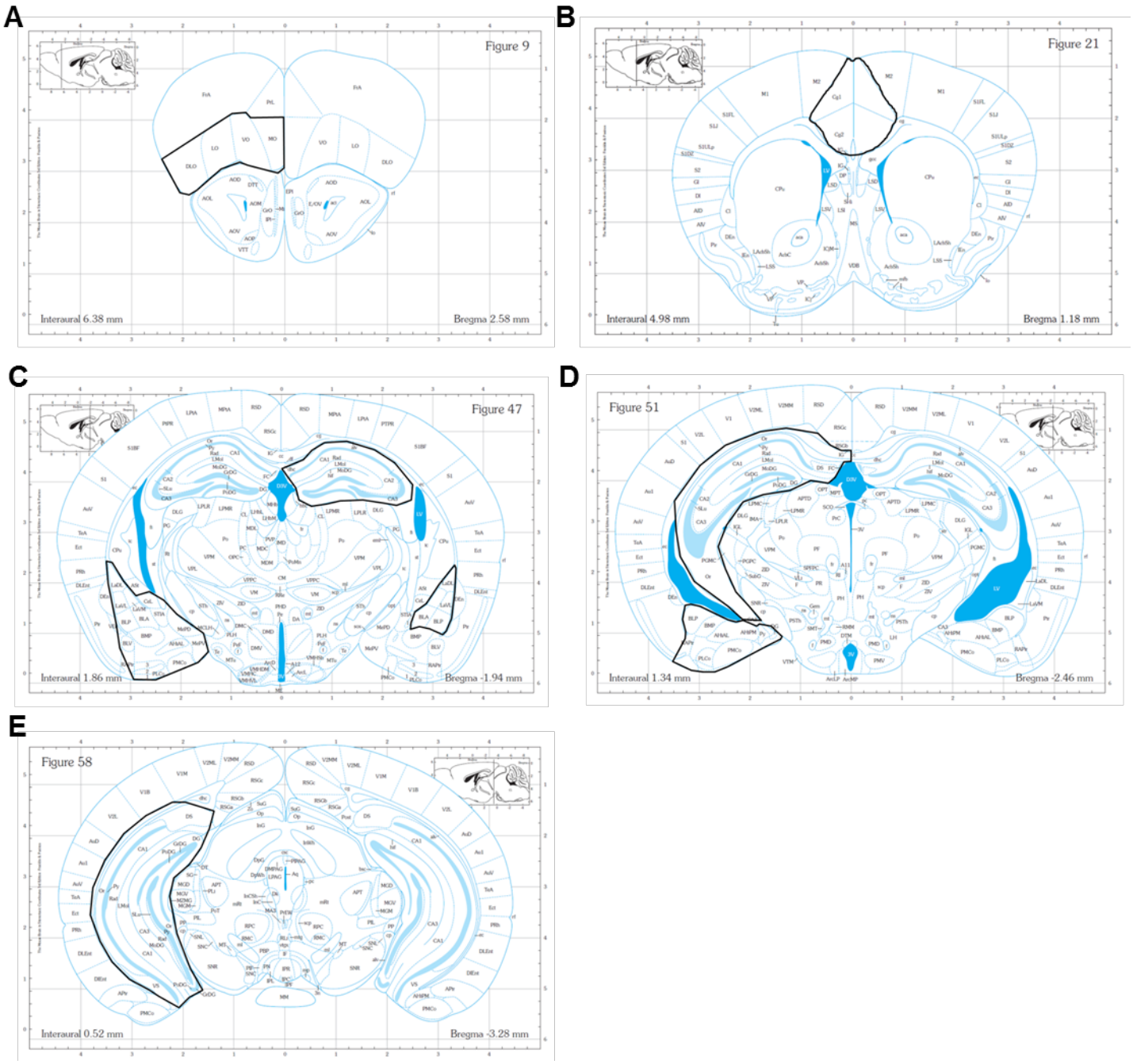

Atlas maps representing manual segmentation of regions of interest (ROI). (**A**) The orbitofrontal cortex ROI. (**B**) The ACC ROI. (**C**) The anterior hippocampus, anterior amygdala and basolateral amygdala ROI. (**D**) The mid hippocampus and posterior amygdala ROI. (**E**) The posterior hippocampus ROI. The atlas maps were used with the permission of the Authors (18).

Supp. Figure 2

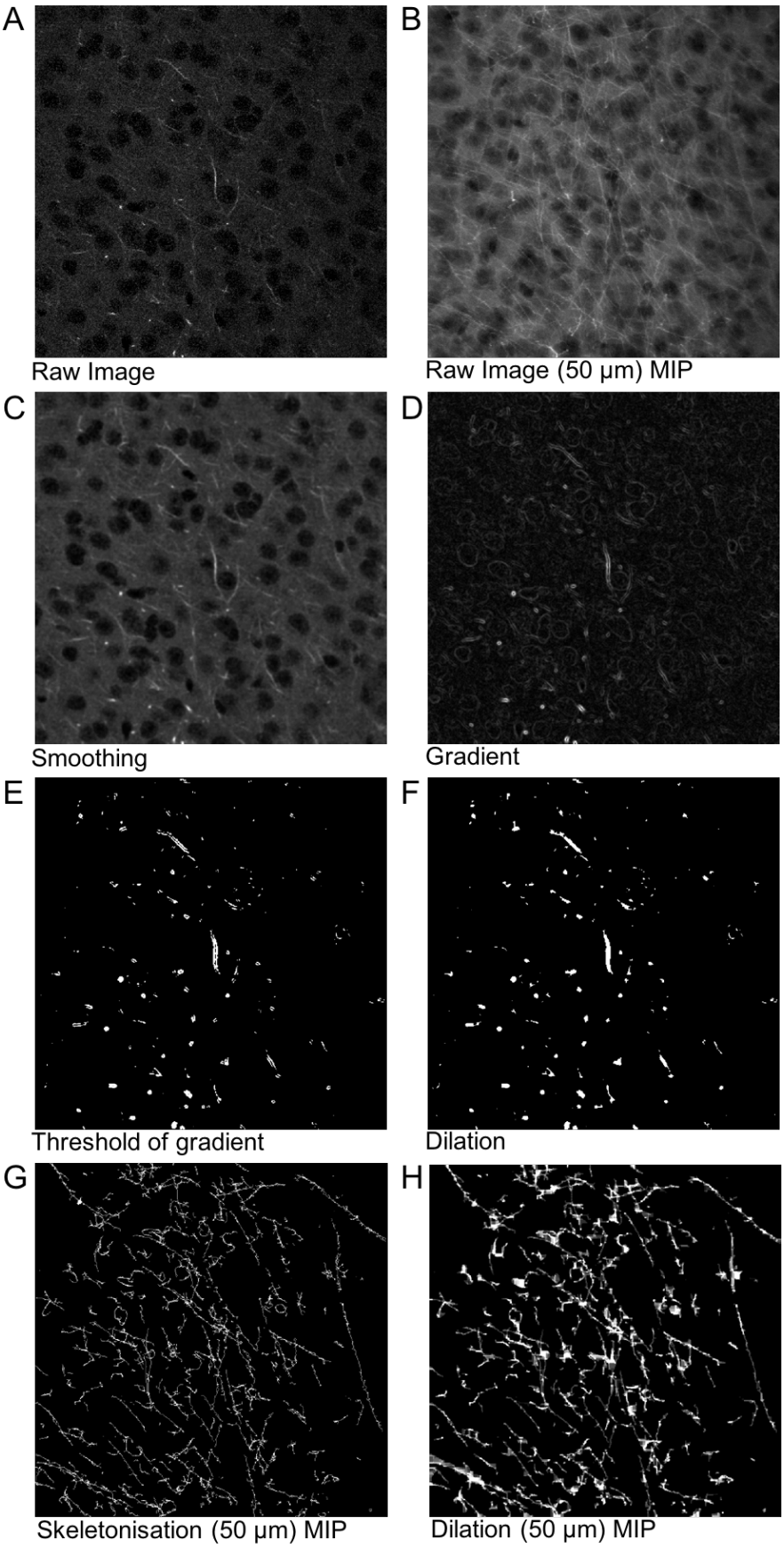

Analysis methodology of axonal segmentation from multiphoton images.

Supp. Figure 3

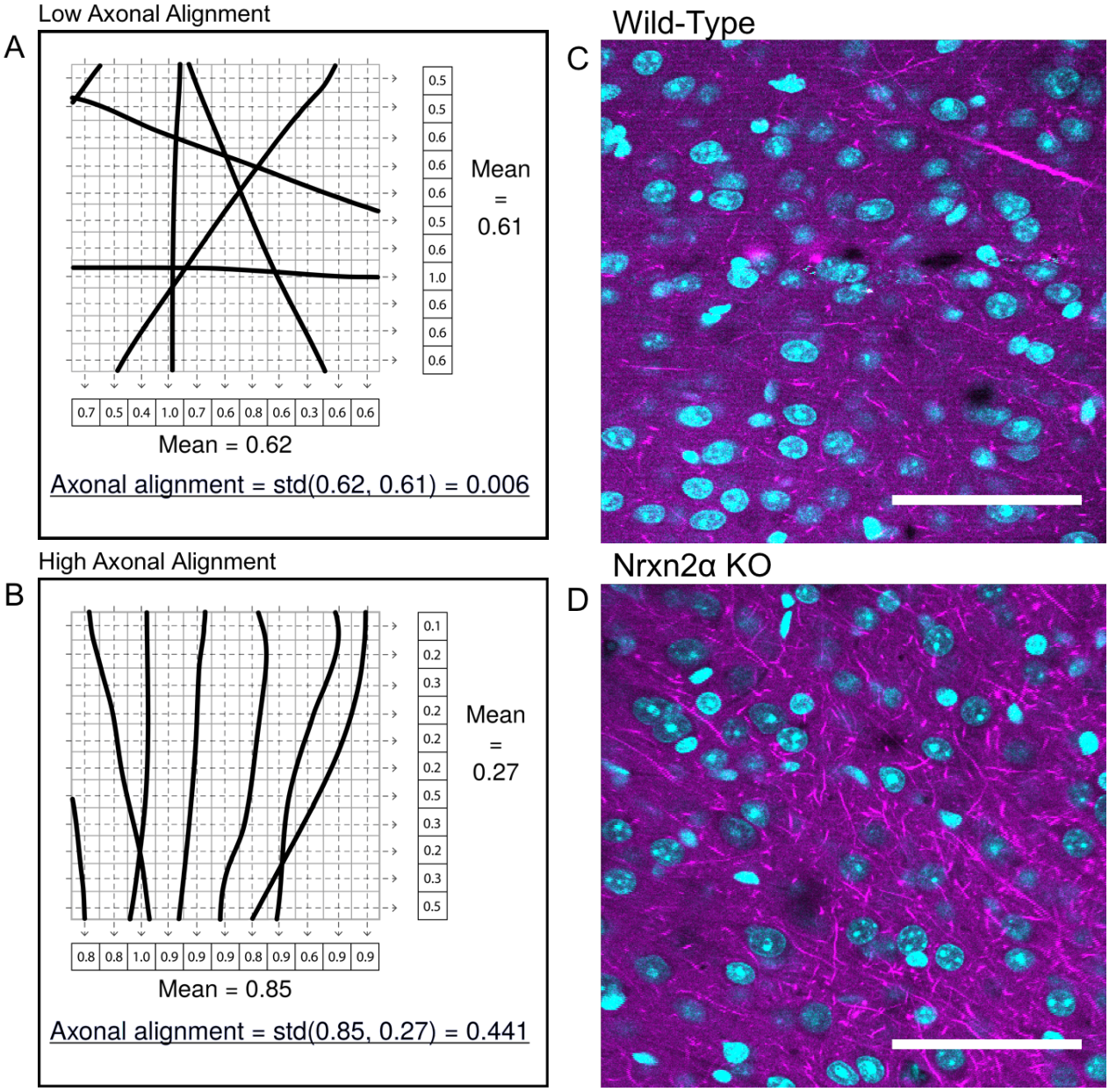

A and B. Illustration of the axonal alignment calculation in a simple two-dimensional case. The grey grid represents the image pixels, the black lines axons and the dashed lines represent the calculation process. Standard deviation denoted as std. **C and D.** Cingulate cortex images taken from wild-type and Nrxn2α KO mice, visually representing the greater axonal alignment and density in KO mice.

Supp. Figure 4

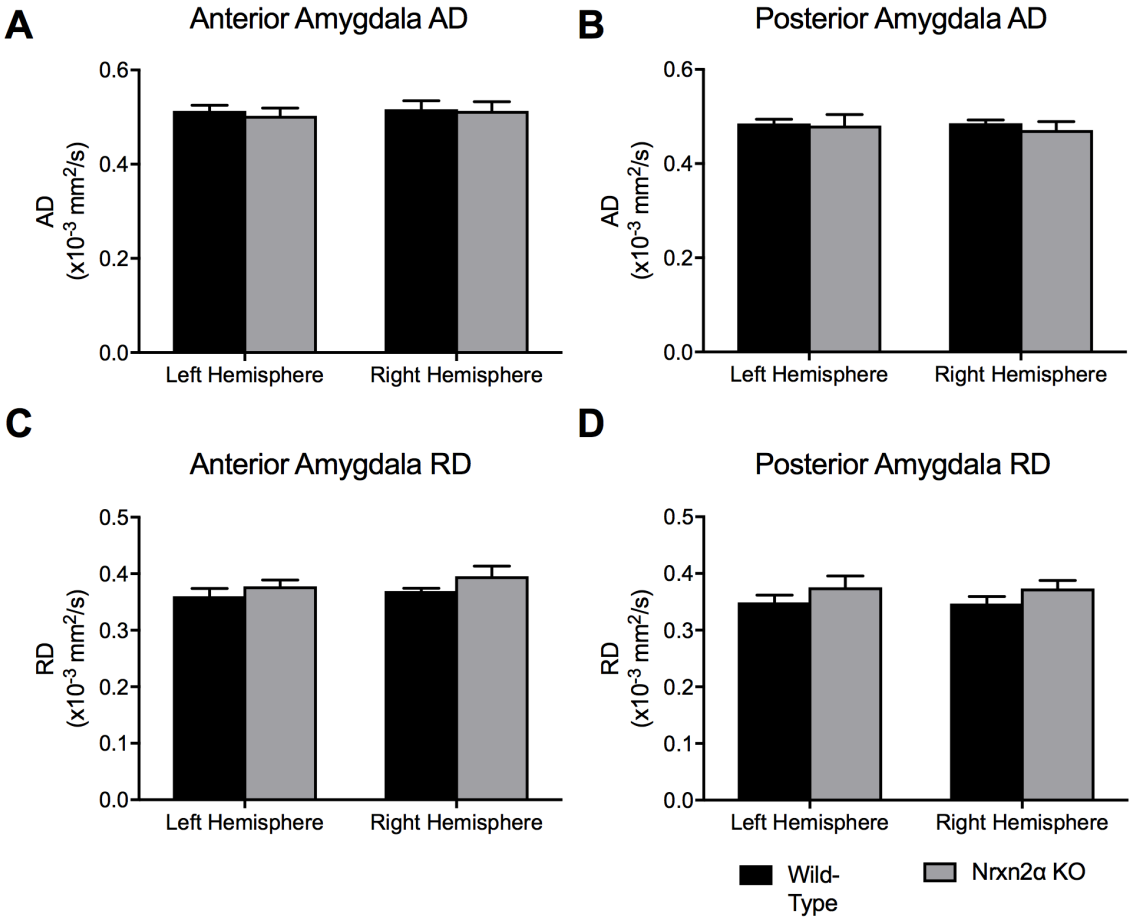

Axial diffusivity (AD) and radial diffusivity (RD) in the amygdala. The entire amygdala was segmented from DTI images at two regions; anterior (**A** and **C**: Bregma -1.94 mm) and posterior (**B** and **D**: Bregma -2.46 mm). No significant differences were observed between the genotypes for anterior or posterior regions. Error bars represent s.e.m. Wild-type n=6, Nrxn2α KO n=6.

Supp. Figure 5

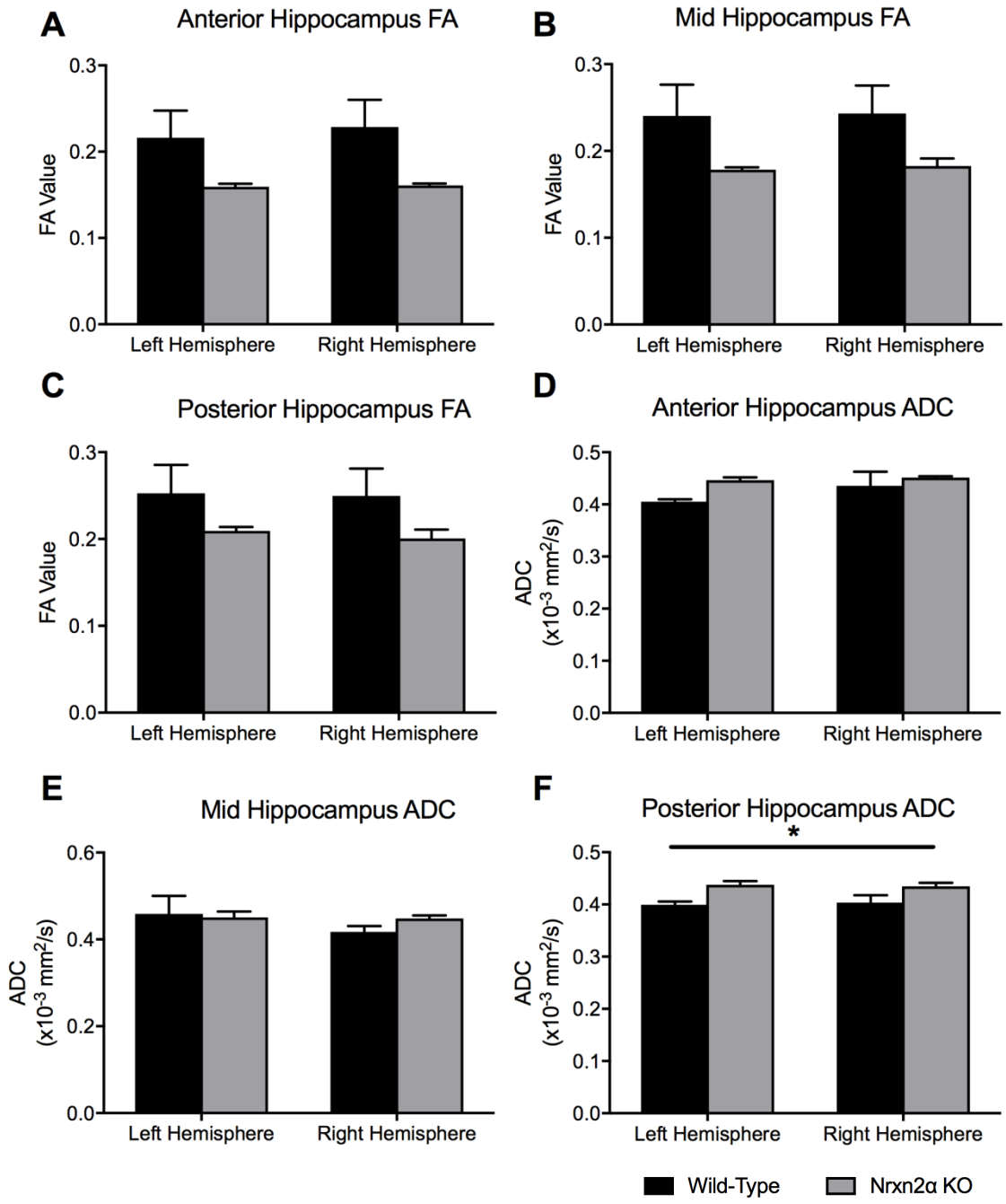

Fractional anisotropy (FA) and apparent diffusion coefficient (ADC) of the anterior to posterior hippocampus. Although Nrxn2α KO had trends towards lower FA in the anterior (**A**), mid (**B**) and posterior (**C**) hippocampus, there were no significant differences. Similarly, anterior (**D**) and mid (**E**) hippocampal regions did not vary between the genotypes, the posterior hippocampus (**F**) had significantly increased ADC (f). * = P<0.05. Error bars represent s.e.m. Wild-type n=6, Nrxn2α KO n=6.

Supp. Figure 6

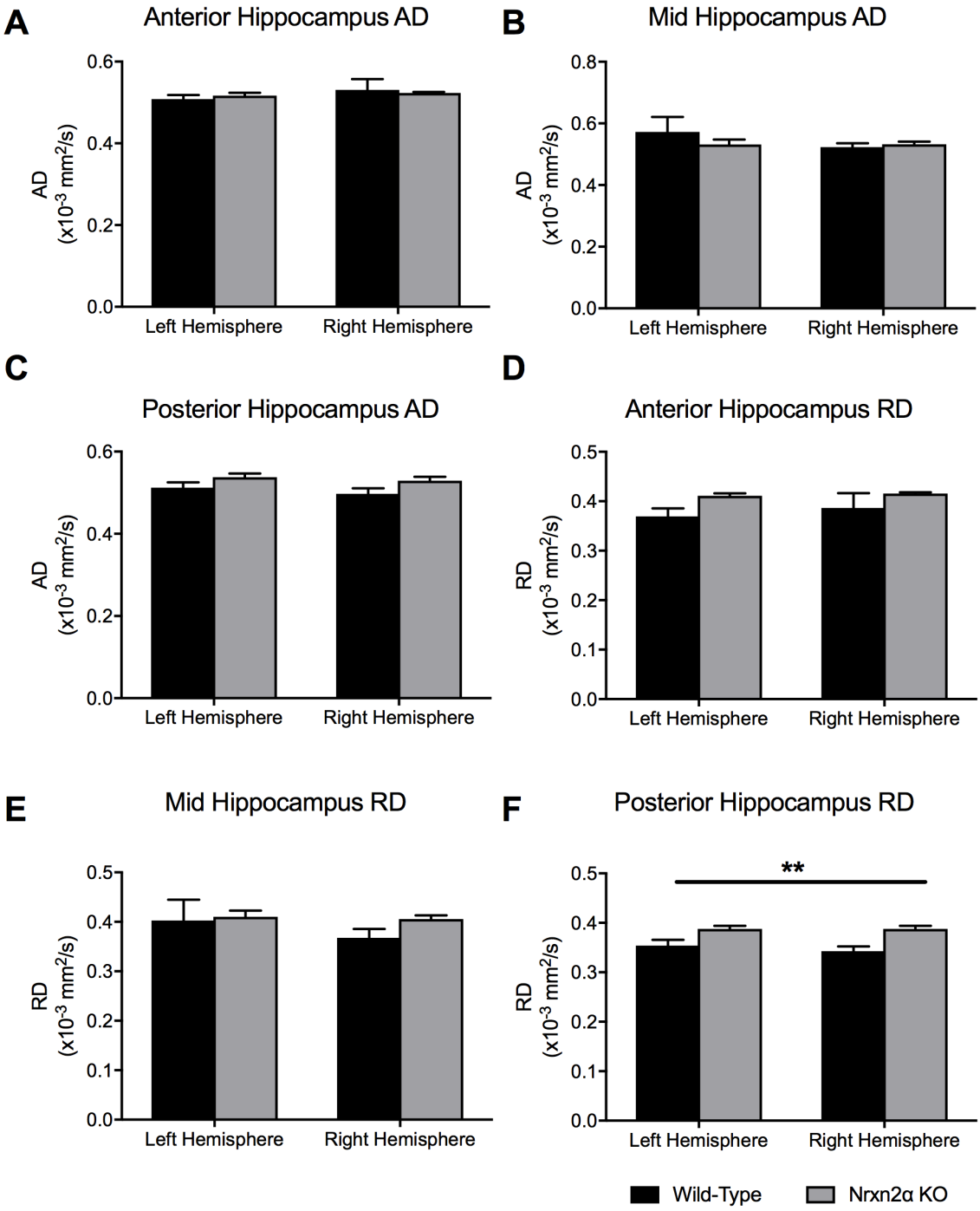

Axial diffusivity (AD) and radial diffusivity (RD) of the anterior to posterior hippocampus. AD did not differ in either the anterior (**A**), mid (**B**) and posterior (**C**) hippocampus. Although the anterior (**D**) and mid (**E**) hippocampal regions did not vary between the genotypes, the posterior hippocampus (**F**) had significantly increased RD (f). ** = P<0.01. Error bars represent s.e.m. Wild-type n=6, Nrxn2α KO n=6.

Supp. Figure 7

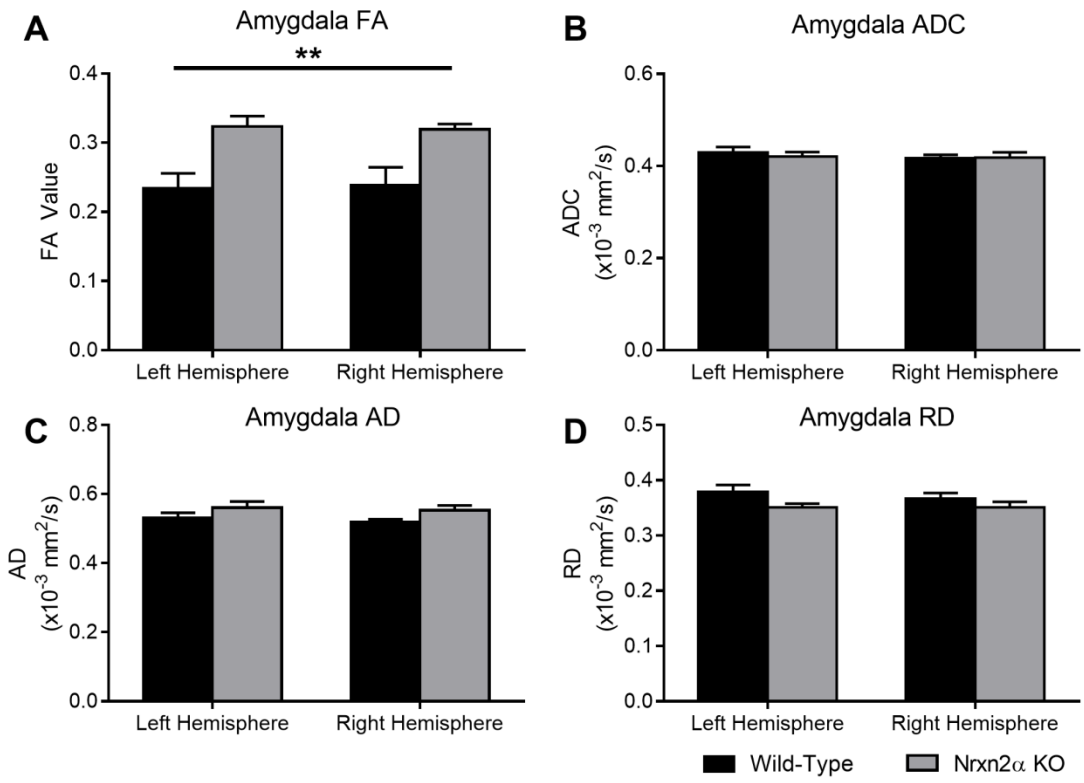

DTI quantified for the whole amygdala volume. (**A**) Fractional anisotropy (FA) was significantly increased in Nrxn2α KO mice (genotype: $F_{(1,10)}$ = 11.15, p = 0.008). However, (**B**) apparent diffusion coefficient (ADC) was not significantly altered (genotype: $F_{(1,10)}$ <1, p = 0.782), nor was (**C**) axial diffusivity (AD) (genotype: $F_{(1,10)}$ = 3.06, p = 0.111) or (**D**) radial diffusivity (RD) (genotype: $F_{(1,10)}$ = 2.47, p = 0.147). Error bars represent s.e.m. ** = P<0.01. Wild-type n=6, Nrxn2α KO n=6.

Supp. Figure 8

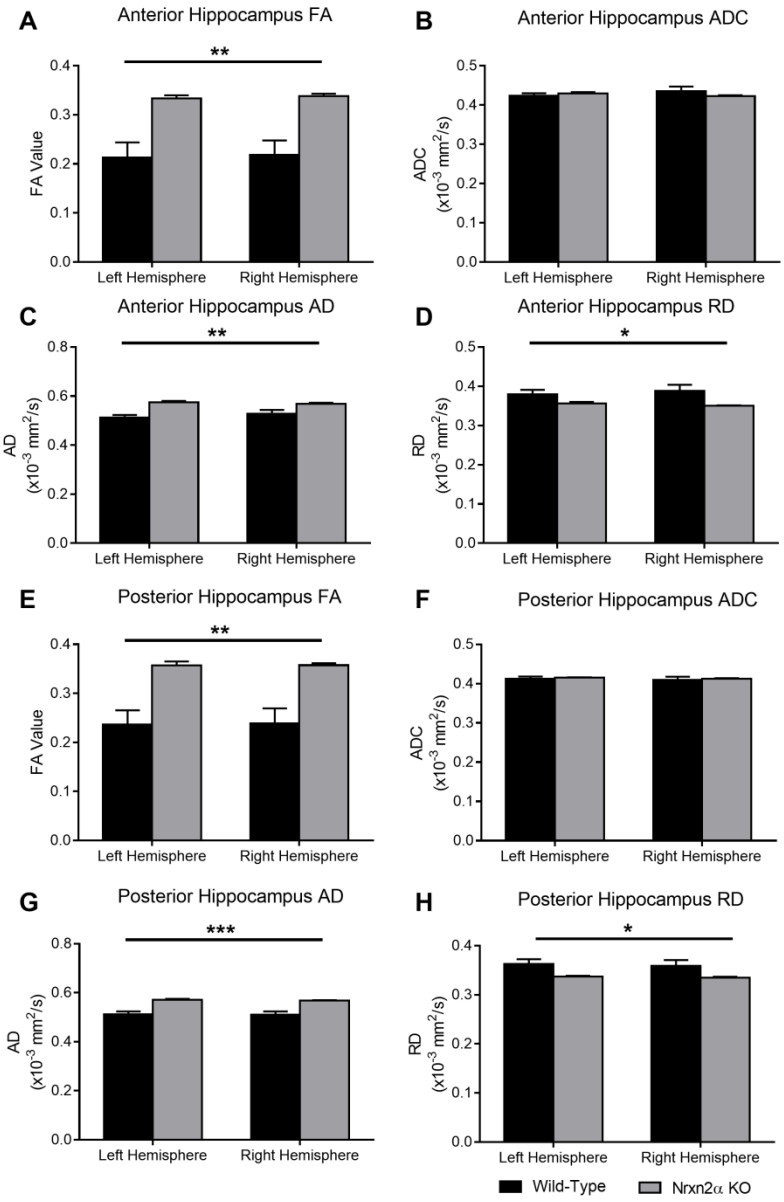

DTI quantified for the whole anterior hippocampus (Bregma -1.06 mm – -2.46 mm) and posterior hippocampus (Bregma -2.54 mm – -3.16 mm). (**A**) Fractional anisotropy (FA) in the anterior hippocampus was significantly increased in Nrxn2α KO mice (genotype: $F_{(1,10)} = 15.63$, $p = 0.0027$) but (**B**) apparent diffusion coefficient (ADC) was not altered (genotype: $F_{(1,10)} < 1$, $p = 0.738$). (**C**) Axial diffusivity (AD) (genotype: $F_{(1,10)} = 16.17$, $p = 0.0024$) and (**D**) radial diffusivity (RD) (genotype: $F_{(1,10)} = 5.05$, $p = 0.048$) were both significantly altered in Nrxn2α KO mice. In the posterior hippocampus, in Nrxn2α KO mice, (**E**) FA was significant increased (genotype: $F_{(1,10)} = 15.62$, $p = 0.0027$), (**F**) ADC was similar to wild-types (genotype: $F_{(1,10)} < 1$, $p = 0.679$), (**G**) AD was increased (genotype: $F_{(1,10)} = 22.31$, $p = 0.0008$) and (**H**) RD was significantly reduced (genotype: $F_{(1,10)} = 5.34$, $p = 0.043$). Error bars represent s.e.m. * = P<0.05, ** = P<0.01, *** = P<0.001. Wild-type n=6, Nrxn2α KO n=6.

Supp. Figure 9

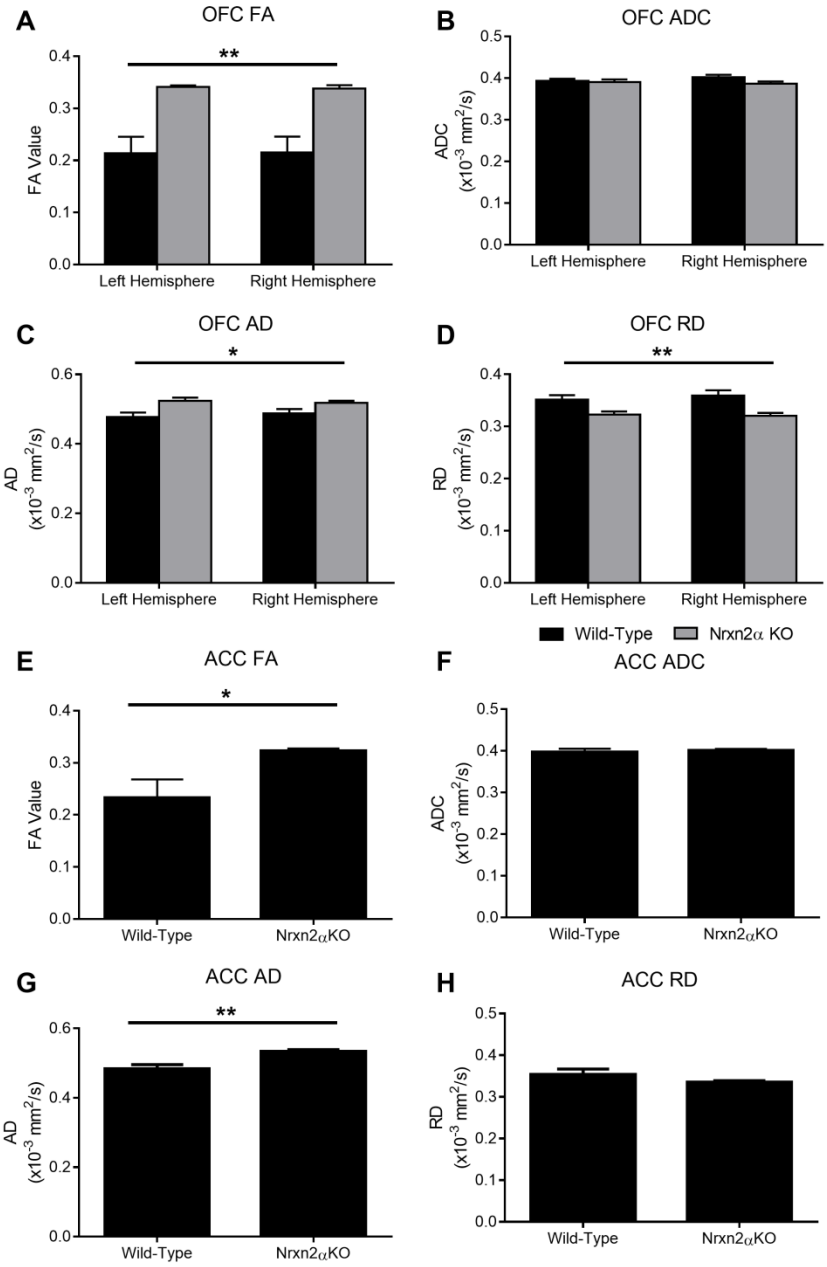

DTI quantified for the whole orbitofrontal cortex (OFC) and anterior cingulate cortex (ACC) and posterior hippocampus (Bregma -1.34 mm – -0.46 mm). (**A**) Fractional anisotropy (FA) in the OFC was significantly increased in Nrxn2α KO mice (genotype: $F_{(1,10)}$ = 16.14, p = 0.0024) but (**B**) apparent diffusion coefficient (ADC) was not altered (genotype: $F_{(1,10)}$ = 1.43, p = 0.260). (**C**) Axial diffusivity (AD) (genotype: $F_{(1,10)}$ = 6.71, p = 0.027) and (**D**) radial diffusivity (RD) (genotype: $F_{(1,10)}$ = 10.07, p = 0.0099) were both significantly altered in Nrxn2α KO mice. In the ACC of Nrxn2α KO mice, (**E**) FA was significant increased (genotype: $t_{(10)}$ = 2.55, p = 0.029), (**F**) ADC was similar to wild-types (genotype: $t_{(10)}$ = 2.55, p = 0.618), (**G**) AD was increased (genotype: $t_{(10)}$ = 3.89, p = 0.003) and (**H**) RD was not significantly different (genotype: $t_{(10)}$ = 1.35, p = 0.208). Error bars represent s.e.m. * = P<0.05, ** = P<0.01. Wild-type n=6, Nrxn2α KO n=6.

Supp. Figure 10

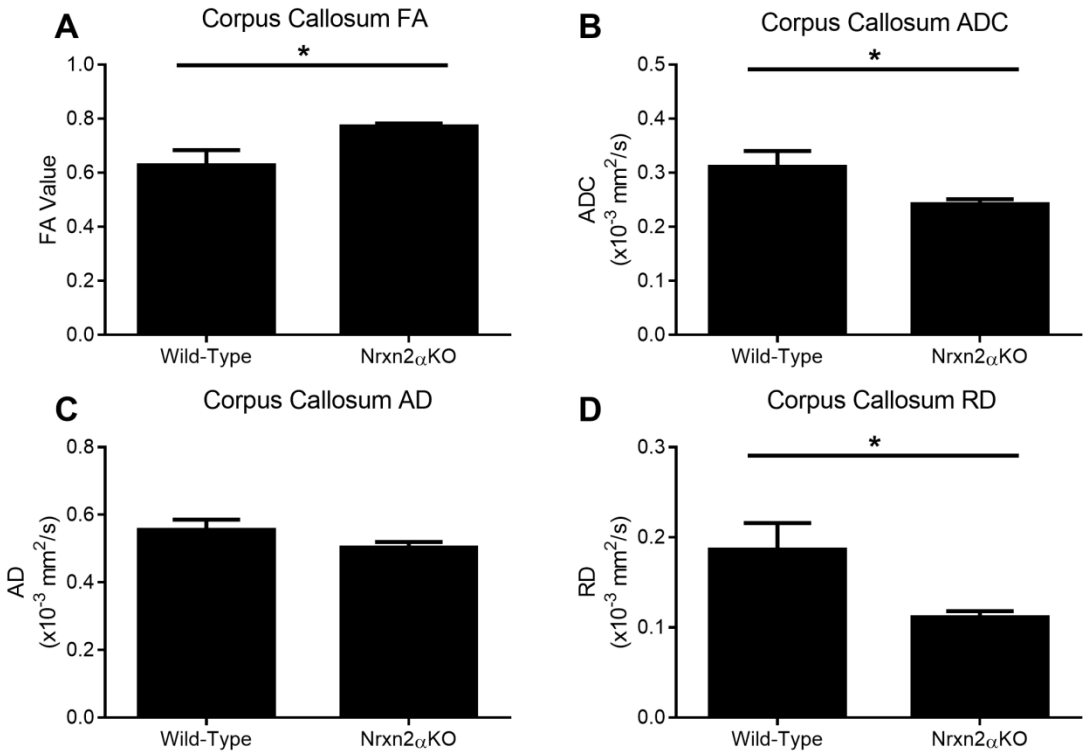

DTI quantification of the corpus callosum (Bregma 0.98 mm). To examine the integrity of white matter tracts within Nrxn2α KO mice, we examined diffusivity in the corpus callosum. (**A**) Fractional anisotropy (FA) was significantly increased in Nrxn2α KO mice (genotype: $t_{(10)} = 2.50$, $p = 0.032$) and apparent diffusion coefficient (ADC) (**B**) significantly decreased (genotype: $t_{(10)} = 2.28$, $p = 0.046$). This difference appeared to be driven predominantly by radial diffusivity (RD), as axial diffusion (AD) (**C**) was not significantly different (genotype: $t_{(10)} = 1.49$, $p = 0.168$) whilst RD (**D**) was significantly reduced in Nrxn2α KO mice (genotype: $t_{(10)} = 2.45$, $p = 0.034$). Error bars represent s.e.m. * = $P<0.05$. Wild-type n=6, Nrxn2α KO n=6.

Supp. Figure 11

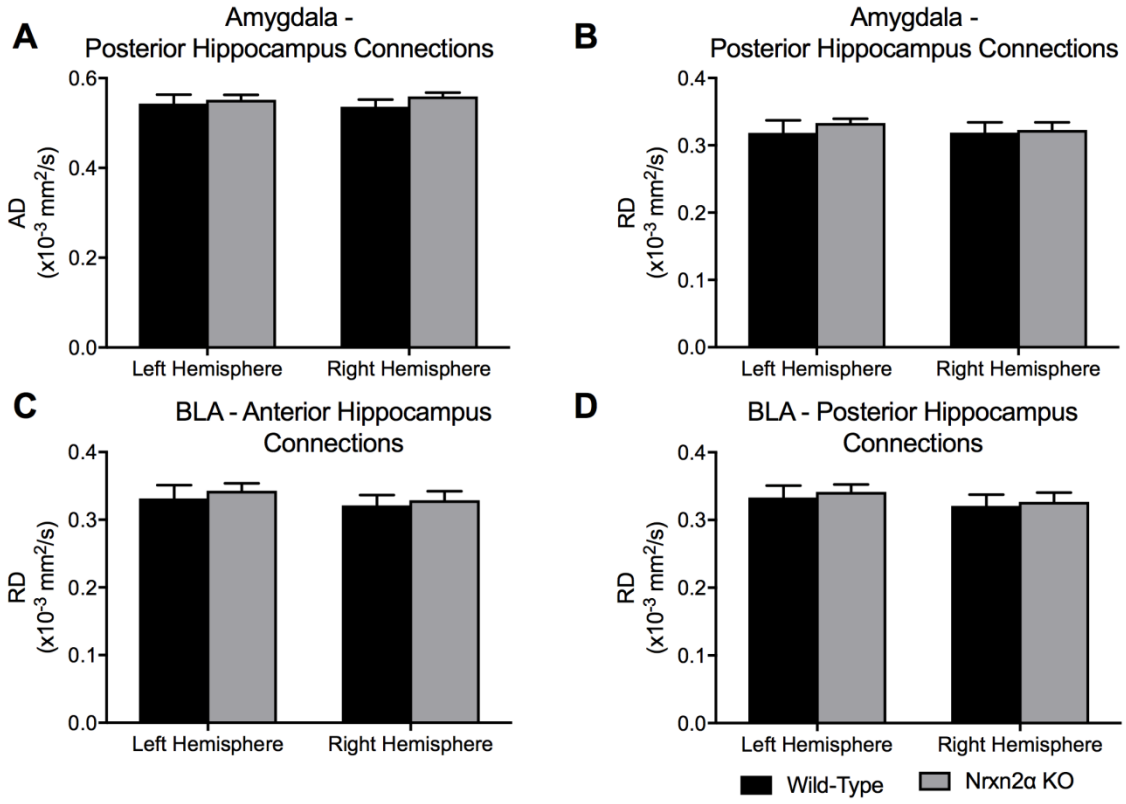

Axial diffusivity (AD) and radial diffusivity (RD) of computed tracts of connections from the amygdala to hippocampus. Tracts from the anterior amygdala to the posterior hippocampus (Bregma -2.46 mm) were analysed for AD (**A**) and RD (**B**). No significant differences between the tracts of Nrxn2α KO mice were observed. No significant differences were found for RD of tracts specifically from the basolateral nuclei of the amygdala (BLA) to the anterior (**C**) or posterior (**D**) hippocampus. Error bars represent s.e.m. Wild-type n=6, Nrxn2α KO n=6.

Supp. Figure 12

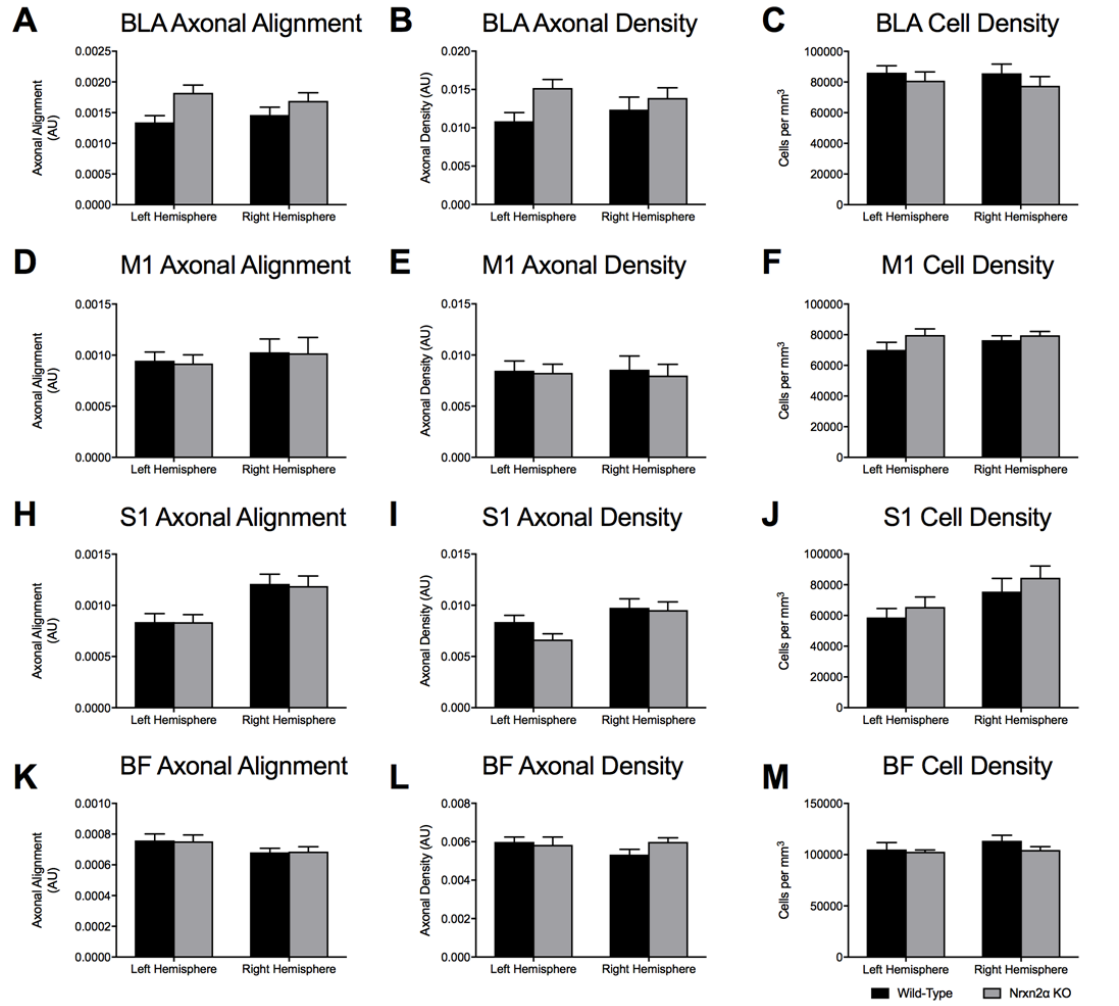

CLARITY-derived quantification of fibres and cell density within the basolateral amygdala (BLA) and control regions (**A**) Although there were trends towards increased axonal alignment and fibre density (**B**) in Nrxn2α KO mice, no significant differences were found. (**C**) Cell density in the BLA was similar between the genotypes. Statistical analysis (Supp. Table 4) was performed for the primary motor cortex (M1; **D-F**), primary somatosensory cortex (S1; **H-J**) and the barrel field (BF; **K-M**). No genotypic differences were found for any measure within these cortical regions. (N-O) CLARITY images of the scanned regions of interest. Error bars represent s.e.m. Wild-type n=6, Nrxn2α KO n=6.

References

1. Wu D, Xu J, McMahon MT, van Zijl PC, Mori S, Northington FJ, et al. In vivo high-resolution diffusion tensor imaging of the mouse brain. NeuroImage. 2013;83:18-26.
2. Vo A, Sako W, Dewey SL, Eidelberg D, Ulug AM. 18FDG-microPET and MR DTI findings in Tor1a+/- heterozygous knock-out mice. Neurobiology of disease. 2015;73:399-406.
3. Kumar M, Duda JT, Hwang WT, Kenworthy C, Ittyerah R, Pickup S, et al. High resolution magnetic resonance imaging for characterization of the neuroligin-3 knock-in mouse model associated with autism spectrum disorder. PloS one. 2014;9(10):e109872.
4. Ruest T, Holmes WM, Barrie JA, Griffiths IR, Anderson TJ, Dewar D, et al. High-resolution diffusion tensor imaging of fixed brain in a mouse model of Pelizaeus-Merzbacher disease: comparison with quantitative measures of white matter pathology. NMR in biomedicine. 2011;24(10):1369-79.
5. Kim S, Pickup S, Fairless AH, Ittyerah R, Dow HC, Abel T, et al. Association between sociability and diffusion tensor imaging in BALB/cJ mice. NMR in biomedicine. 2012;25(1):104-12.
6. Jones DK. The effect of gradient sampling schemes on measures derived from diffusion tensor MRI: a Monte Carlo study. Magnetic resonance in medicine. 2004;51(4):807-15.
7. Lebel C, Benner T, Beaulieu C. Six is enough? Comparison of diffusion parameters measured using six or more diffusion-encoding gradient directions with deterministic tractography. Magnetic resonance in medicine. 2012;68(2):474-83.
8. Ni H, Kavcic V, Zhu T, Ekholm S, Zhong J. Effects of number of diffusion gradient directions on derived diffusion tensor imaging indices in human brain. AJNR American journal of neuroradiology. 2006;27(8):1776-81.
9. Hasan KM, Parker DL, Alexander AL. Comparison of gradient encoding schemes for diffusion-tensor MRI. Journal of magnetic resonance imaging : JMRI. 2001;13(5):769-80.
10. Schindelin J, Arganda-Carreras I, Frise E, Kaynig V, Longair M, Pietzsch T, et al. Fiji: an open-source platform for biological-image analysis. Nature methods. 2012;9(7):676-82.
11. Peng H, Ruan Z, Long F, Simpson JH, Myers EW. V3D enables real-time 3D visualization and quantitative analysis of large-scale biological image data sets. Nature biotechnology. 2010;28(4):348-53.
12. Linkert M, Rueden CT, Allan C, Burel JM, Moore W, Patterson A, et al. Metadata matters: access to image data in the real world. The Journal of cell biology. 2010;189(5):777-82.
13. Perge JA, Niven JE, Mugnaini E, Balasubramanian V, Sterling P. Why do axons differ in caliber? The Journal of neuroscience : the official journal of the Society for Neuroscience. 2012;32(2):626-38.
14. Otsu N. A Threshold Selection Method from Gray-Level Histograms. IEEE Transactions on Systems, Man, and Cybernetics. 1979;9(1):62-6.
15. Rosin P. Unimodal thresholding. Pattern Recognition. 2001;34(11):2083-96.
16. Lee T, Kashyap R, Chu C. Building Skeleton Models via 3-D Medial Surface Axis Thinning Algorithms. CVGIP: Graphical Models and Image Processing. 1994;56(6):462-78.
17. Kerschnitzki M, Kollmannsberger P, Burghammer M, Duda GN, Weinkamer R, Wagermaier W, et al. Architecture of the osteocyte network correlates with bone material quality. Journal of bone and mineral research : the official journal of the American Society for Bone and Mineral Research. 2013;28(8):1837-45.
18. Franklin K, Paxinos G. The Mouse Brain in Stereotaxic Coordinates: Academic Press; 2008.

Figure 1

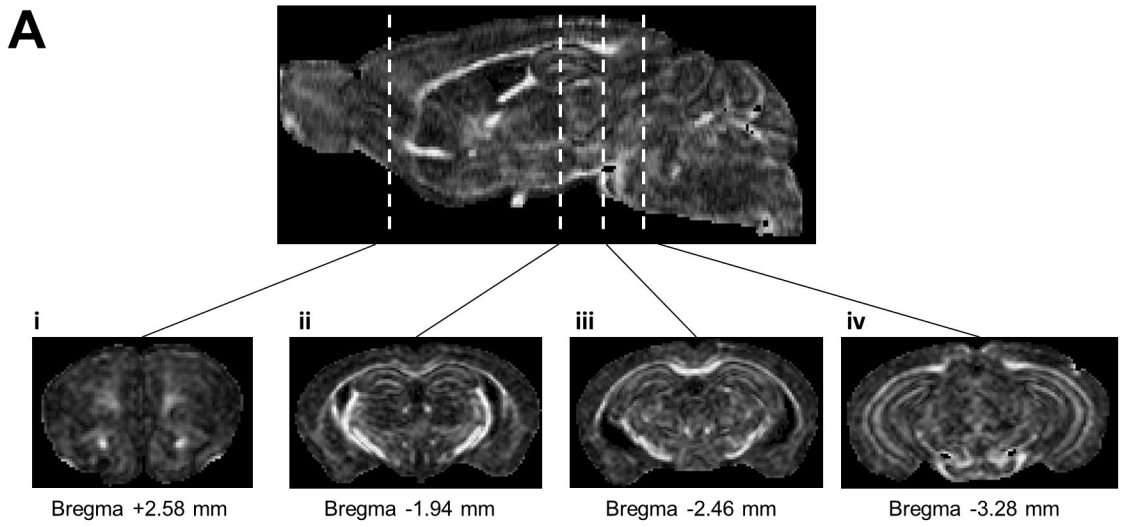
A
i
ii
iii
iv
Bregma +2.58 mm
Bregma -1.94 mm
Bregma -2.46 mm
Bregma -3.28 mm

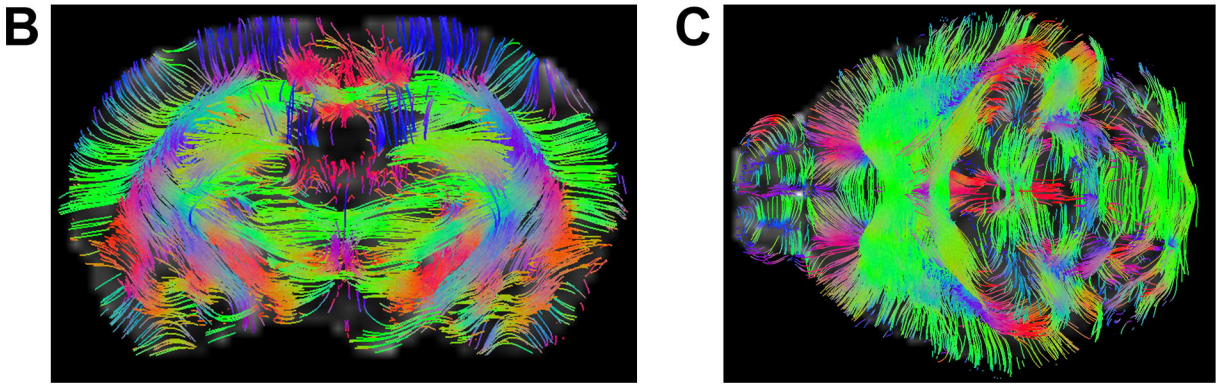
B
C

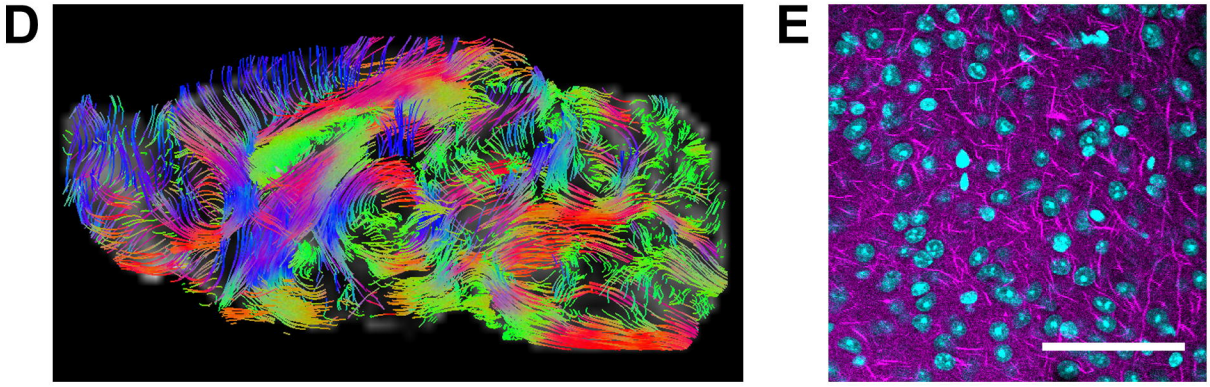
D
E

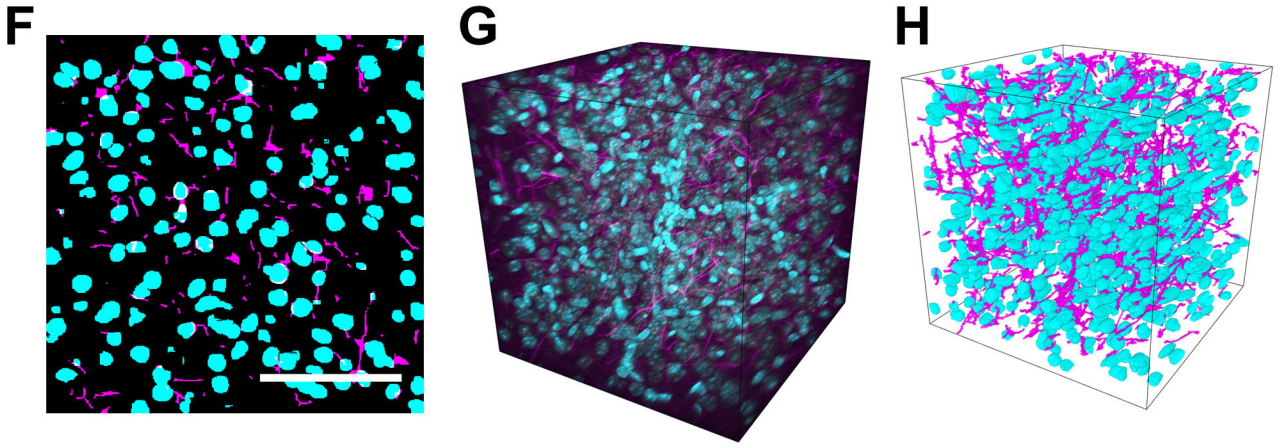
F
G
H

Figure 2

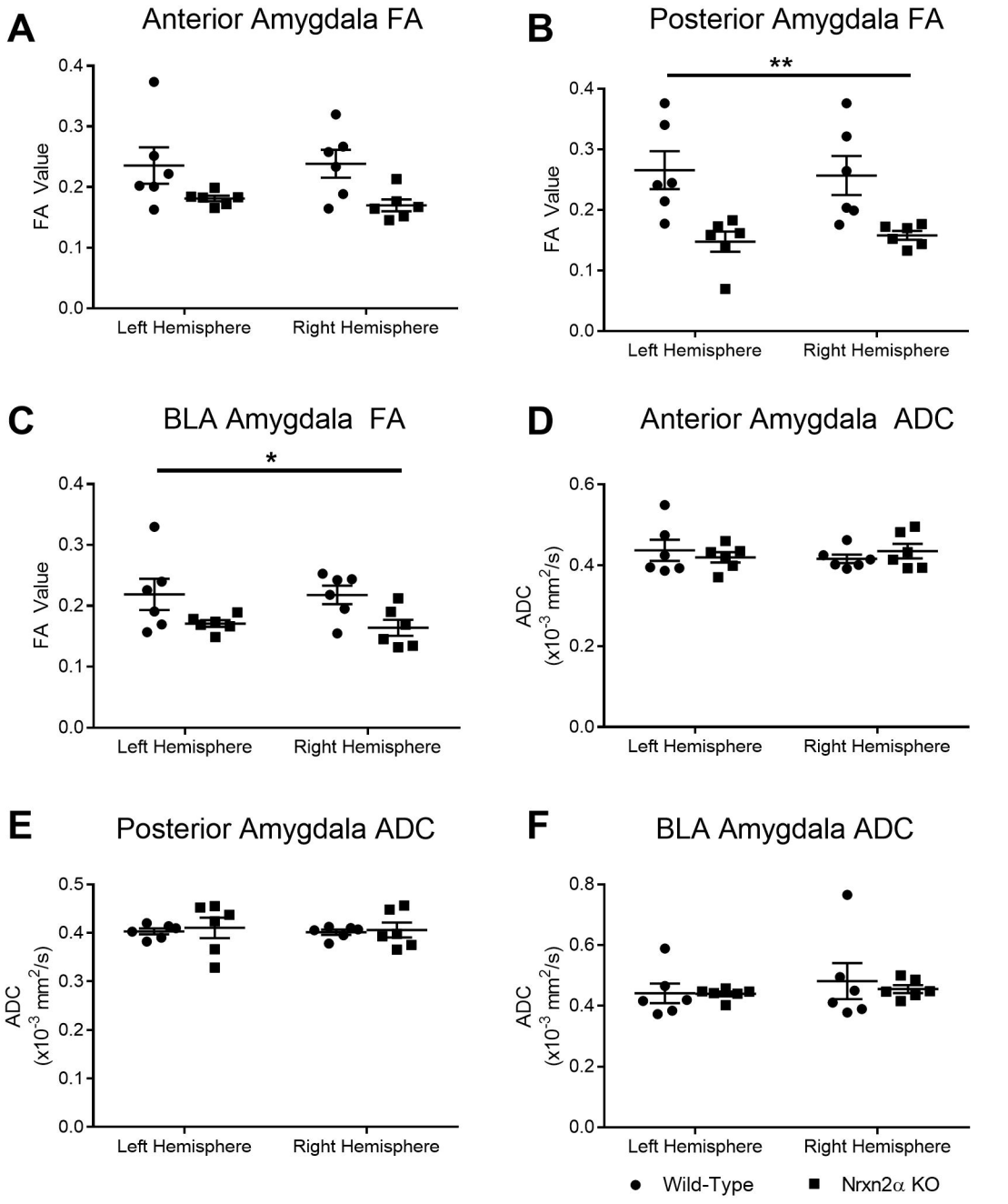
A
Anterior Amygdala FA
FA Value
0.4
0.3
0.2
0.1
0.0
Left Hemisphere
Right Hemisphere
B
Posterior Amygdala FA
**
FA Value
0.4
0.3
0.2
0.1
0.0
Left Hemisphere
Right Hemisphere
C
BLA Amygdala FA
*
FA Value
0.4
0.3
0.2
0.1
0.0
Left Hemisphere
Right Hemisphere
D
Anterior Amygdala ADC
ADC
(x10-3 mm2/s)
0.6
0.4
0.2
0.0
Left Hemisphere
Right Hemisphere
E
Posterior Amygdala ADC
ADC
(x10-3 mm2/s)
0.5
0.4
0.3
0.2
0.1
0.0
Left Hemisphere
Right Hemisphere
F
BLA Amygdala ADC
ADC
(x10-3 mm2/s)
0.8
0.6
0.4
0.2
0.0
Left Hemisphere
Right Hemisphere
Wild-Type
Nrxn2α KO

Figure 3

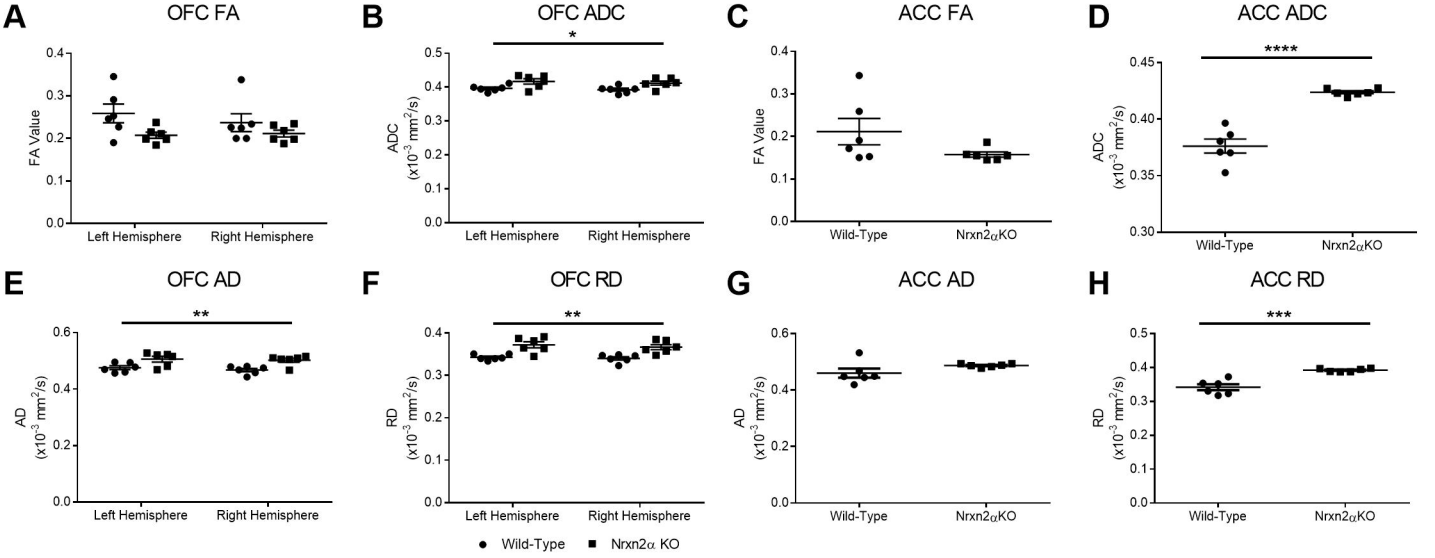
A
OFC FA
FA Value
0.4
0.3
0.2
0.1
0.0
Left Hemisphere
Right Hemisphere
B
OFC ADC
*
ADC
(x10-3 mm2/s)
0.5
0.4
0.3
0.2
0.1
0.0
Left Hemisphere
Right Hemisphere
C
ACC FA
FA Value
0.4
0.3
0.2
0.1
0.0
Wild-Type
Nrxn2αKO
D
ACC ADC
****
ADC
(x10-3 mm2/s)
0.45
0.40
0.35
0.30
Wild-Type
Nrxn2αKO
E
OFC AD
**
AD
(x10-3 mm2/s)
0.6
0.4
0.2
0.0
Left Hemisphere
Right Hemisphere
F
OFC RD
**
RD
(x10-3 mm2/s)
0.4
0.3
0.2
0.1
0.0
Left Hemisphere
Right Hemisphere
Wild-Type
Nrxn2α KO
G
ACC AD
AD
(x10-3 mm2/s)
0.6
0.4
0.2
0.0
Wild-Type
Nrxn2αKO
H
ACC RD
***
RD
(x10-3 mm2/s)
0.5
0.4
0.3
0.2
0.1
0.0
Wild-Type
Nrxn2αKO

Figure 4

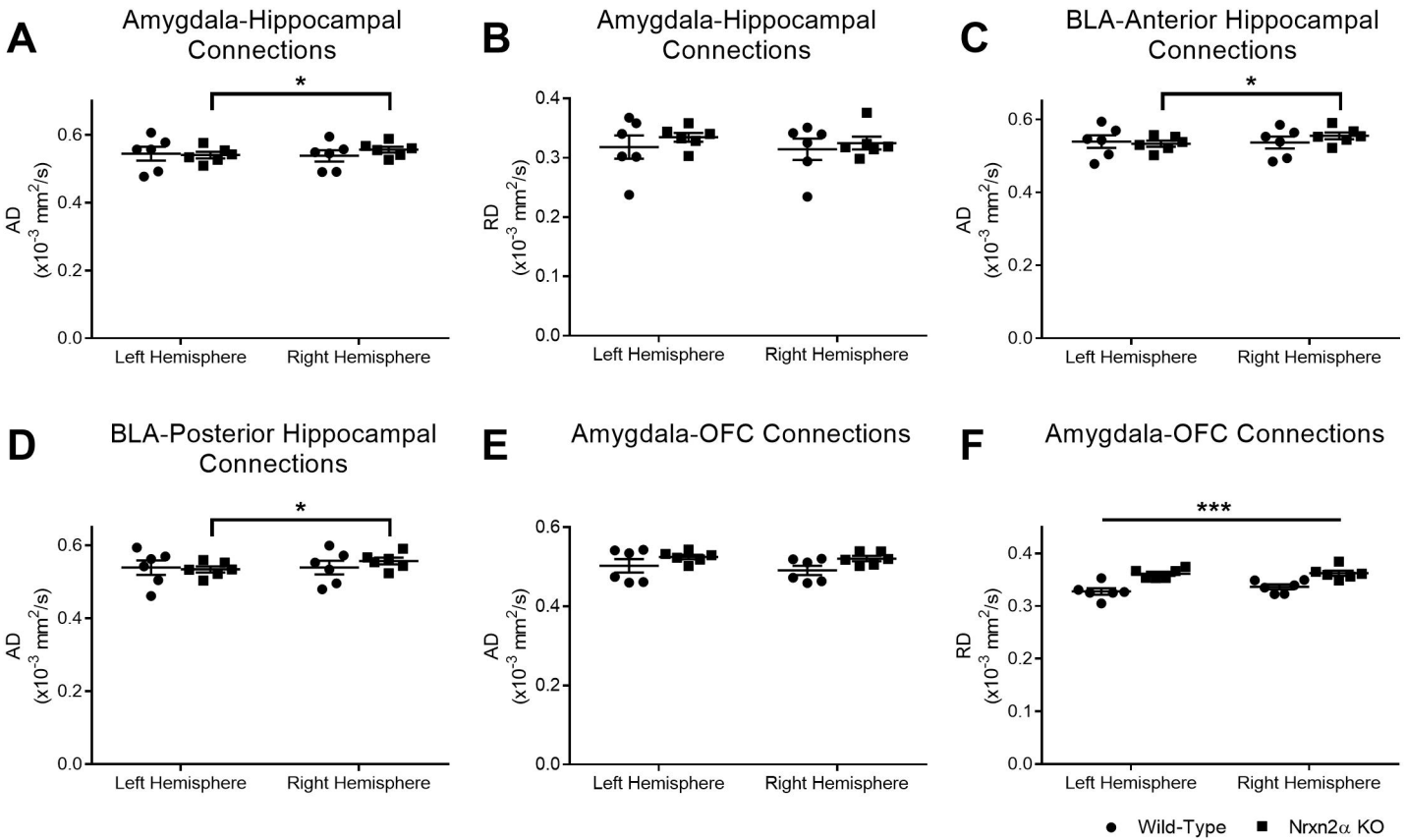
A
Amygdala-Hippocampal Connections
*
AD (x10-3 mm2/s)
0.0
0.2
0.4
0.6
Left Hemisphere
Right Hemisphere
B
Amygdala-Hippocampal Connections
RD (x10-3 mm2/s)
0.0
0.1
0.2
0.3
0.4
Left Hemisphere
Right Hemisphere
C
BLA-Anterior Hippocampal Connections
*
AD (x10-3 mm2/s)
0.0
0.2
0.4
0.6
Left Hemisphere
Right Hemisphere
D
BLA-Posterior Hippocampal Connections
*
AD (x10-3 mm2/s)
0.0
0.2
0.4
0.6
Left Hemisphere
Right Hemisphere
E
Amygdala-OFC Connections
AD (x10-3 mm2/s)
0.0
0.2
0.4
0.6
Left Hemisphere
Right Hemisphere
F
Amygdala-OFC Connections
***
RD (x10-3 mm2/s)
0.0
0.1
0.2
0.3
0.4
Left Hemisphere
Right Hemisphere
Wild-Type
Nrxn2α KO

Figure 5

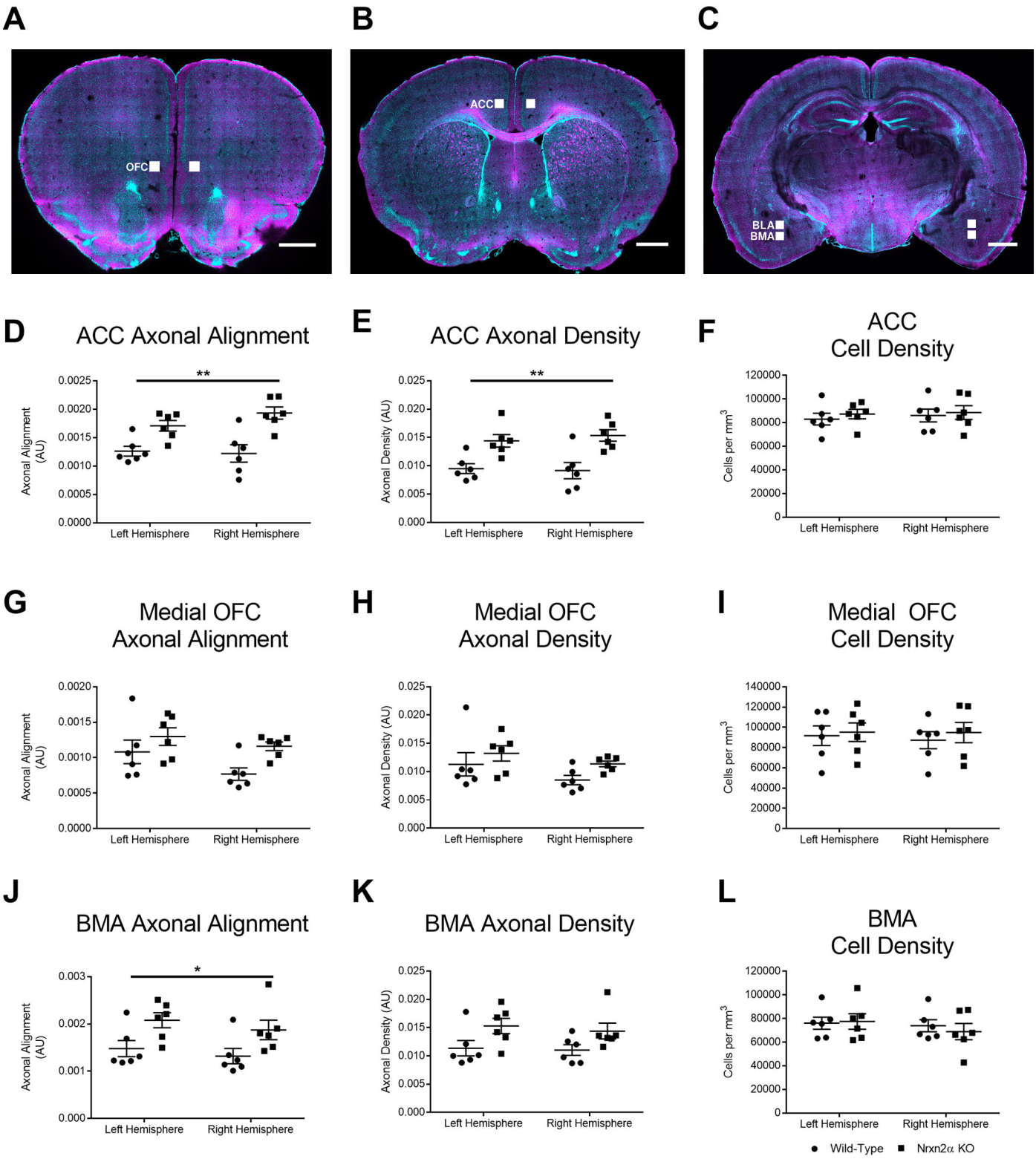
A
B
C
OFC
ACC
BLA
BMA
D
ACC Axonal Alignment
Axonal Alignment (AU)
0.0025
0.0020
0.0015
0.0010
0.0005
0.0000
**
Left Hemisphere
Right Hemisphere
E
ACC Axonal Density
Axonal Density (AU)
0.025
0.020
0.015
0.010
0.005
0.000
**
Left Hemisphere
Right Hemisphere
F
ACC
Cell Density
Cells per mm3
120000
100000
80000
60000
40000
20000
0
Left Hemisphere
Right Hemisphere
G
Medial OFC
Axonal Alignment
Axonal Alignment (AU)
0.0020
0.0015
0.0010
0.0005
0.0000
Left Hemisphere
Right Hemisphere
H
Medial OFC
Axonal Density
Axonal Density (AU)
0.025
0.020
0.015
0.010
0.005
0.000
Left Hemisphere
Right Hemisphere
I
Medial OFC
Cell Density
Cells per mm3
140000
120000
100000
80000
60000
40000
20000
0
Left Hemisphere
Right Hemisphere
J
BMA Axonal Alignment
Axonal Alignment (AU)
0.003
0.002
0.001
0.000
*
Left Hemisphere
Right Hemisphere
K
BMA Axonal Density
Axonal Density (AU)
0.025
0.020
0.015
0.010
0.005
0.000
Left Hemisphere
Right Hemisphere
L
BMA
Cell Density
Cells per mm3
120000
100000
80000
60000
40000
20000
0
Left Hemisphere
Right Hemisphere
Wild-Type
Nrxn2α KO